LOW EARTH ORBITAL ATOMIC OXYGEN, MICROMETEOROID, AND DEBRIS INTERACTIONS WITH PHOTOVOLTAIC ARRAYS

Bruce A. Banks, Sharon K. Rutledge, and Kim K. de Groh
NASA Lewis Research Center
Cleveland, Ohio

SUMMARY

Polyimide Kapton solar array blankets can be protected from atomic oxygen in low earth orbit if SiO_X thin film coatings are applied to their surfaces. The useful lifetime of a blanket protected in this manner strongly depends upon the number and size of defects in the protective coatings. Atomic oxygen degradation is dominated by undercutting at defects in protective coatings caused by substrate roughness and processing rather than micrometeoroid or debris impacts. This is due to the low flux of debris and micrometeoroid impact particles of significant size. Recent findings from the Long Duration Exposure Facility (LDEF) and ground-based studies show that interactions between atomic oxygen and silicones may cause crazing and contamination problems which may lead to solar array degradation.

INTRODUCTION

Atomic oxygen is formed in the low-earth-orbital (LEO) environment through photodissociation of O_2 by solar photons having wavelengths shorter than 2430Å. Because of the low probability of atomic oxygen interaction with neighboring atoms or molecules, it remains atomic in its 3p ground state rather than re-associating. Spacecraft such as Space Station Freedom (SSF), will collide with this LEO atomic oxygen atmosphere with impingement energies of 4.5 ± 1 eV (ref. 1.). As a result of this atomic oxygen bombardment, oxidation of unprotected polyimide Kapton, which is a structural support member for the solar array, would result in unacceptably low durability of the solar array blanket. No suitable materials have been found to date as replacements for solar array blankets which possess both the desirable properties of polyimide Kapton and have acceptable durability to atomic oxygen. Metal oxide protective coatings such as SiO_X, and other metal oxides including fluoropolymer filled metal oxides (for improved strain to failure) have been identified as suitable materials to provide atomic oxygen protection to underlying polyimide Kapton (ref. 2-4). The durability of SiO_X-protected Kapton depends strongly upon the number and size of defects in the coating which allow atomic oxygen to react with the underlying polyimide Kapton.

Other materials used in the fabrication of flexible solar arrays such as silicones react with atomic oxygen to develop an SiO_2 protective surface layer; however, crazing of the surface and deposition on adjoining surfaces from the silicone present durability and contamination concerns.

ATOMIC OXYGEN

Low Earth Orbital Environment

The characteristics of the LEO atomic oxygen environment which significantly influence the rate of oxidation of exposed polymeric materials are the energy, flux, and angle of attack of the impinging atomic oxygen. The full-width-at-half-maximum energy spread of approximately 2 eV for a mean ram energy of 4.5 eV (at altitudes of 400 kilometers) is the result of both the Maxwell Boltzman distribution of hot (approximately 1000 K) atomic oxygen and the spacecraft orbital inclination with respect to the earth's atmospheric rotation direction (ref. 1). The atomic oxygen fluence is strongly dependent on the altitude, solar activity, and time of day with respect to solar noon. Table I lists the atomic oxygen durability requirements for SSF surfaces. These requirements

represent worst case scenarios with a high atomic oxygen fluence to assure 15 year solar array durability (ref. 5). Atomic oxygen fluence to surfaces which are not perpendicular to the ram direction is approximately proportional to the cosine of the angle of attack as shown in Figure 1 (for 400 km altitude) for angles below 80°. Beyond 80° the arriving fluence is significantly elevated above a cosine dependence because the high temperature Maxwell Boltzman distribution contributes impinging velocity vectors which can be at various angles with respect to the ram direction. In addition, the earth's atmospheric co-rotation produces a sinusoidally varying velocity vector orientation because of the typical orbital inclination of 28.5°. The total consequence of the various velocity vector contributors is that surfaces 90° to the orbital ram direction are exposed to fluences which are 4.1% of the ram fluence as shown in Figure 1 (ref. 6).

Interactions with Array Materials

Atomic oxygen protection of the SSF Kapton solar array blankets is to be achieved by RF magnetron sputter-deposited 1300Å-thick coatings of SiO_X (where X is between 1.9 and 2.0) applied to each side of two sheets of 0.00254 cm thick Kapton H sheets which are clad together with a silicone adhesive (McGahn Nusil CV-2502) containing a fiberglass scrim (Figure 2). The purpose of the fiberglass scrim in the silicone adhesive is to provide structural integrity to the clad Kapton blanket through load transference even after significant atomic oxygen degradation. Degradation of the solar array blanket by atomic oxygen occurs chiefly at defects in the SiO_X-protective coatings. Such defects are typically pin windows or scratches in the protective coating which allow atomic oxygen to attack the underlying Kapton material. Defects can arise as a result of the initial uncoated Kapton roughness or surface irregularities, contamination, abrasion during SiO_X sputter deposition, flexure or abrasion during flexible circuit processing, or from micrometeoroid and debris impact in space. Such coatings have been found to possess approximately 1000 defects per cm^2. The atomic oxygen durability of the protective coatings can be assessed using RF plasma discharges in air or oxygen to simulate LEO atomic oxygen degradation. Figure 3 shows the percent mass remaining of SiO_X-coated Kapton as a function of effective atomic oxygen fluence in an asher operated with air. Some of the coatings have total defect areas which are so large that they cannot survive the desired SSF 15-year fluence requirement of 4.85×10^{22} atoms/cm^2 for the average of solar and antisolar facing surfaces of the array. Differences in the rate of mass loss in test coupons appears to be strongly dependent on the number and size of atomic oxygen defects in the protective coatings. Figure 4a is a scanning electron micrograph of a SiO_X-protected Kapton surface after atomic oxygen exposure to an effective fluence of 1×10^{21} atoms/cm^2 in an RF plasma asher. Figure 4b shows the same location after tape was used to remove the SiO_X coating. As can be seen in Figure 4b, atomic oxygen undercutting at the site of pin windows and scratches is clearly evident even in places where little evidence of atomic oxygen undercutting can be seen in Figure 4a. If the applied protective coating is free from residual stress, undercutting of the coating can occur without the coating tearing. If sufficient stress exists to cause the coating to tear when undercut, significantly more atomic oxygen will be allowed to enter the defect causing accelerated damage to the underlying Kapton. The shape of the undercut cavities below pin windows is highly dependent upon the directional characteristics of the atomic oxygen arrival. Figure 5 illustrates the initial shape of atomic oxygen undercutting resulting from isotropic RF plasma atomic oxygen arrival, directed beam or fixed ram atomic oxygen arrival, and sweeping ram arrival. Functional solar arrays will be exposed to sweeping ram atomic oxygen arrival, which should produce an initial atomic oxygen undercut geometry which is elongated in shape. As the atomic oxygen oxidizes all the way through the Kapton to the SiO_X coating on the opposite side of the sheet, significantly more scattering of the atomic oxygen will occur, which should be more closely replicated by the plasma asher environment than by fixed arrival direction exposures. Thus with time, undercutting patterns at pin window defect sites should evolve to nearly circular symmetry.

Evidence of atomic oxygen undercutting in space, even for ram atomic oxygen arrival, can be seen from the results of aluminized Kapton multilayer insulation exposed on the LDEF spacecraft. Figure 6 shows aluminized Kapton from the LDEF spacecraft which was exposed to an estimated fluence of 5.77×10^{21} atoms/cm^2, both prior to (Fig 6a) and after (Fig 6b) removal of the aluminum coating. Projections of durability of solar array material exposed to sweeping atomic oxygen arrival conditions as anticipated by SSF may be accomplished

from ground based plasma asher and directed beam simulations as well as with in-space directed ram exposure experiments such as the LDEF spacecraft. By comparison of ground and space based data, Monte Carlo models can be created and used to project performance of arrays in space (ref. 7).

Silicone adhesives are used extensively in the construction of the SSF solar array, as shown in Figure 2. Portions of the silicone (Dow Corning 93-500) adhesives used to attach the cover glass to the solar cells will be exposed to atomic oxygen attack. If significant degradation of the Kapton circuit carrier sheet or Kapton overlay sheet occurs, then exposure of the cladding silicone adhesive (McGahn Nusil CV-2502) may occur. In addition, silicones are used for thermal control of solar array diode surfaces. Although silicones tend to develop SiO_2-protective outer layers, high fluence atomic oxygen exposure tends to cause silicones to develop tensile stresses in the near surface layers, causing crazing, which can extend deep into the silicone bulk. As such crazing advances, secondary branch cracks also develop. Figure 7 is a scanning electron micrograph of silicone adhesive (from Kapton adhesive tape) exposed on the LDEF spacecraft to an estimated fluence of 4.92×10^{21} atoms/cm^2. In addition to crazing, silicones eject polymeric fragments during atomic oxygen attack which contaminate adjoining surfaces. This contaminant layer develops as a brown coating where further atomic oxygen bombards the contaminated surfaces. Figure 8 is a photograph of a portion of the Solar-Array-Materials Passive LDEF experiment (A0171) which contained samples of silicones (ref. 8). To the immediate right side of the light-colored silicone samples in the center of the photograph are clear regions followed by dark deposits (further to the right) where atomic oxygen impingement occurred. Similar dark contaminant layers have been observed in ground plasma asher tests. This LDEF experiment was located on row A8 which had atomic oxygen arriving from 38° to the left of the surface normal. Figure 9 illustrates the transference and observed dark contamination which results from further atomic oxygen bombardment of the ejected silicone polymeric fragments. Little is known about the surface mobility of the atomic oxygen ejected silicone molecular fragments; however, extensive silicone contamination has been observed on LDEF surfaces. The role of ultraviolet solar illumination on contamination issues is not fully clear, based on LDEF and plasma asher results to date. If ejected silicone polymeric fragments can transport themselves to the front surface of solar cell cover glasses then atomic oxygen darkening could degrade solar array output through darkening around the perimeter of each cell. Figure 10 illustrates how atomic oxygen might reach the silicone cover glass adhesive allowing ejected silicone contaminants to redeposit on adjoining surfaces.

MICROMETEOROIDS AND DEBRIS

The flux of particles of a given diameter and smaller that arrive on surfaces characteristic of the SSF orbital environment is shown in Figure 11 (ref. 9). The flux of micrometeoroid particles is surpassed by debris particles for particles of diameter less than 10^{-3} cm. Large diameter particles can create large defects in the protective coatings on solar array blankets. However, the flux of large particles is not sufficient to contribute to substantial oxidative solar array mass loss from subsequent atomic oxygen attack. Smaller particles, though more frequent in number, produce crater areas which are negligibly small for particles below 10^{-5} cm in diameter (ref. 9). The fractional mass loss, $\Delta M/M$, of the SSF solar array blanket, due to atomic oxygen attack at debris-caused defect sites, can be shown to be approximated by:

$$\frac{\Delta M}{M} = \frac{\pi k}{2y} \left(\frac{R^2 d^2}{4} - x^2 \right) d^{-2.5} f E t^2$$

where: k = constant = $2.82 \times 10^{-17}(cm)^{0.5}/sec$ (ref 9)
R = ratio of crater to debris particle diameter
d = debris particle diameter, cm
x = SiO_X protective coating thickness, cm
f = atomic oxygen flux, atoms/cm^2/sec
E = Kapton atomic oxygen erosion yield, cm^3/atom
t = mission duration , sec
y = Kapton thickness, cm

For R = 5 (ref. 10), x = 1.3×10^{-5} cm (1300Å), f = 1.14×10^{14} atom/cm^2/sec (ref. 5), E = 3.0×10^{-24} cm^3/atom (ref. 1), t = 4.73×10^8 sec (15 yrs.), and y = 0.00254 cm;

The mass loss of the antisolar facing Kapton overlay is calculated to be only 0.2% of the initial mass after 15 years in low earth orbit. If one assumes that the debris-caused atomic oxygen defects have extensive atomic oxygen undercutting, then the atomic oxygen reaction probability may be near 1 due to multiple scattering, producing erosion yields near $2.2 \times 10^{-23}cm^3$/atom. Even with such an assumption, the percent mass loss of the Kapton overlay would still represent only 1.4% of the initial blanket mass. Although debris particles ($\geq 10^{-5}$ cm in diameter) appear to be the largest contributor to the number of defects (approximately 3000/cm^2/yr), the area of damage caused by these particles is far less than the area of pin windows and scratches (approximately 1000 defects/cm^2) resulting from the Kapton roughness, deposition of the coating, and from flexible circuit processing. Because the micrometeoroid flux is significantly below the debris flux for 10^{-5} to 10^{-4} cm diameter particles, micrometeoroids do not represent a life-limiting hazard to the atomic oxygen durability of solar array blankets. Results of micrometeoroid or debris particle impacts on SiO_X-protective coatings has been witnessed on the LDEF spacecraft as show in Figure 12. As can be seen from Figure 12, cracking of the glass coating is limited to the vicinity of the impact site, even for this rather large diameter crater.

CONCLUSIONS

Atomic oxygen protective coatings, such as sputter deposited SiO_X, are inherently durable to low-earth-orbital atomic oxygen attack. Defects in these coatings caused as a result of surface roughness, coating deposition, processing, or micrometeoroid and debris impact will allow atomic oxygen to attack the underlying polyimide Kapton material. The atomic oxygen durability of current SiO_X-deposited coatings indicates that initial roughness, coating deposition, and processing-caused defects dominate the atomic oxygen degradation processes. Micrometeoroid and debris impacts do not constitute a threat to the atomic oxygen durability of solar array blankets. Potential atomic oxygen interaction with silicones must be considered to determine whether or not crazing and contamination associated with atomic oxygen interactions will cause solar array degradation.

REFERENCES

1. Banks, Bruce A., Rutledge, Sharon K., Auer, Bruce A., and DiFilippo, Frank, "Atomic Oxygen Undercutting of Defects on SiO_2 Protected Polyimide Solar Array Blankets," Proceedings of the Materials Degradation in Low Earth Orbit Symposium of the 119th TMS Annual Meeting and Exhibit, Anaheim, CA, February 18-22, 1990.

2. Banks, Bruce A., Mirtich, Michael J., Rutledge, Sharon K., and Nahra, Henry K., "Protection of Solar Array Blankets from Attack by Low Earth Orbital Atomic Oxygen," Proceedings of the 18th IEEE Photovoltaic Specialist Conference, October 21-25, 1985, Las Vegas, NV.

3. Banks, Bruce, A., Mirtich, Michael J., Sovey, James S., Nahra, Henry K., and Rutledge, Sharon K., "Flexible Fluoropolymer Filled SiO_2 Protective Coatings," Presented at the Technology 2000 Conference, Washington, D.C., November 27-28, 1990.

4. Rutledge, Sharon K. and Mihelcic, Judith A., "Undercutting of Defects in Thin Film Protective Coatings on Polymer Surfaces Exposed to Atomic Oxygen," NASA TM 101986, Presented at the 16th International Conference on Metallurgical Coatings, American Vacuum Society, San Diego, CA, April 17-21, 1989.

5. Rockwell International Corporation SSF document RC1800, section 3.2.5.1.1.3 atomic oxygen, January 10, 1991.

6. Bourassa, Roger J. and Gillis, James R., "Data Summary: Atomic Oxygen Flux and Fluence Calculation for Long Duration Exposure Facility (LDEF), NAS1-18224, task 12, LDEF Materials Data Analysis, Boeing Defense and Space Group, Seattle, WA, August 13, 1990.

7. Banks, Bruce A., Auer, Bruce M., Rutledge, Sharon K. and Hill, Carol M., "Atomic Oxygen Interaction with Solar Array Blankets at Protective Coating Defect Sites," Presented at the 4th Annual Workshop on Space Operations, Automation and Robotics (SOAR 90), Albuquerque, NM, June 26-28, 1990.

8. Clark, Linwood, Kinard, William, Carter, David, Jones, James Jr., "The Long Duration Exposure Facility (LDEF) Mission One Experiments," NASA SP-4731984.

9. Space Station Program Natural Environment Definition for Design, Change request SSP-30425, January, 1991.

10. Carey, W. C., McDonnell, J., and Dixon, D. "An Empirical Penetration Equation for Thin Metallic Films Used in Capture Cell Techniques" in Properties and Interactions of Interplanetary Dust, pp. 131-136, published by D. Reidel Publishing Co., 1985.

TABLE I. - ATOMIC OXYGEN DURABILITY REQUIREMENTS FOR THE SSF PHOTOVOLTAIC ARRAY

Surface	Atomic Oxygen Flux, atoms/cm^2 sec	Atomic Oxygen 15 year Fluence, atoms/cm^2
Ram Facing	3.6×10^{14}	1.7×10^{23}
Solar Facing	9.1×10^{13}	4.31×10^{22}
Anti-Solar Facing	1.14×10^{14}	5.40×10^{22}
Average of Solar and Anti-Solar Facing	1.02×10^{14}	4.85×10^{22}

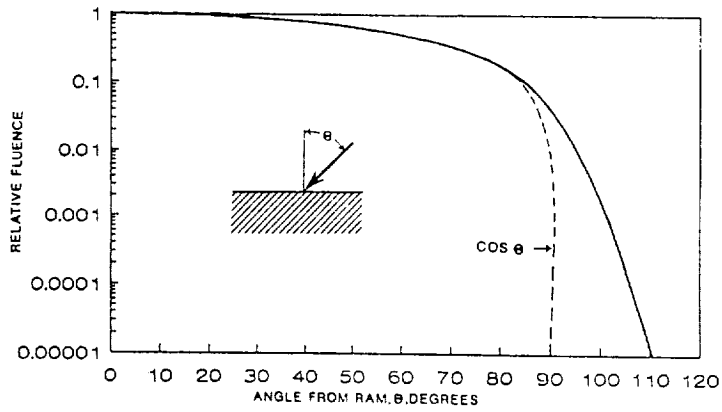

Figure 1: Atomic oxygen fluence dependence on arrival angle.

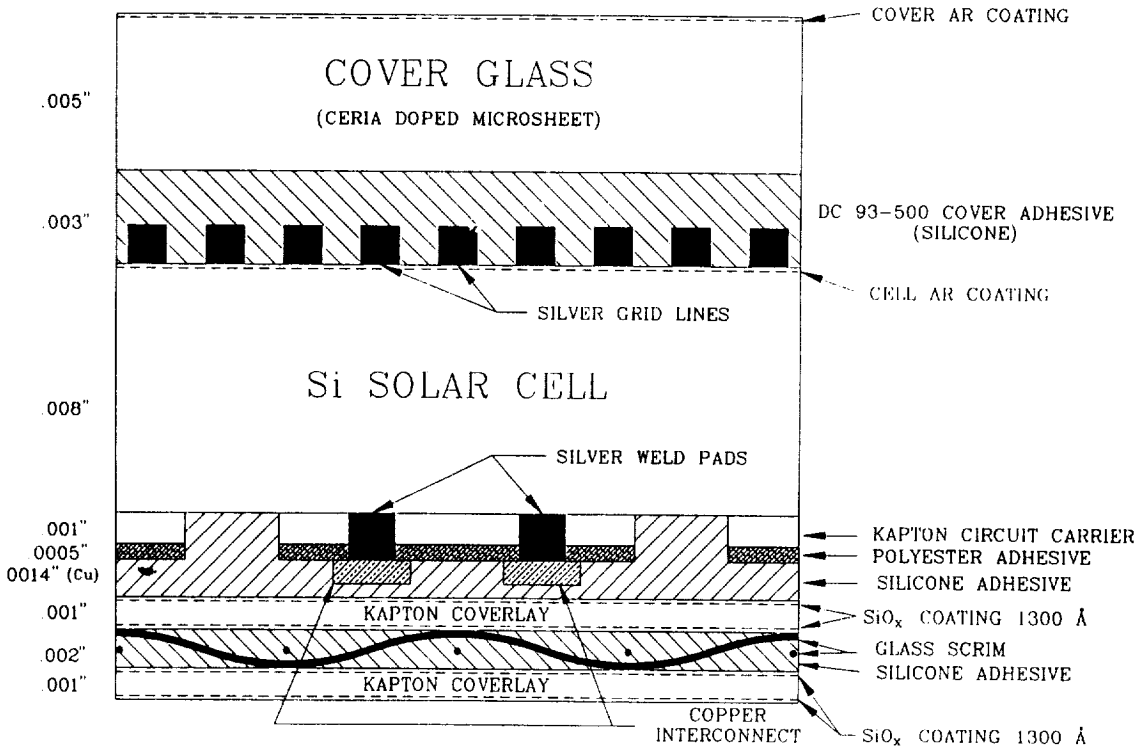

Figure 2: SSF solar array blanket cross section.

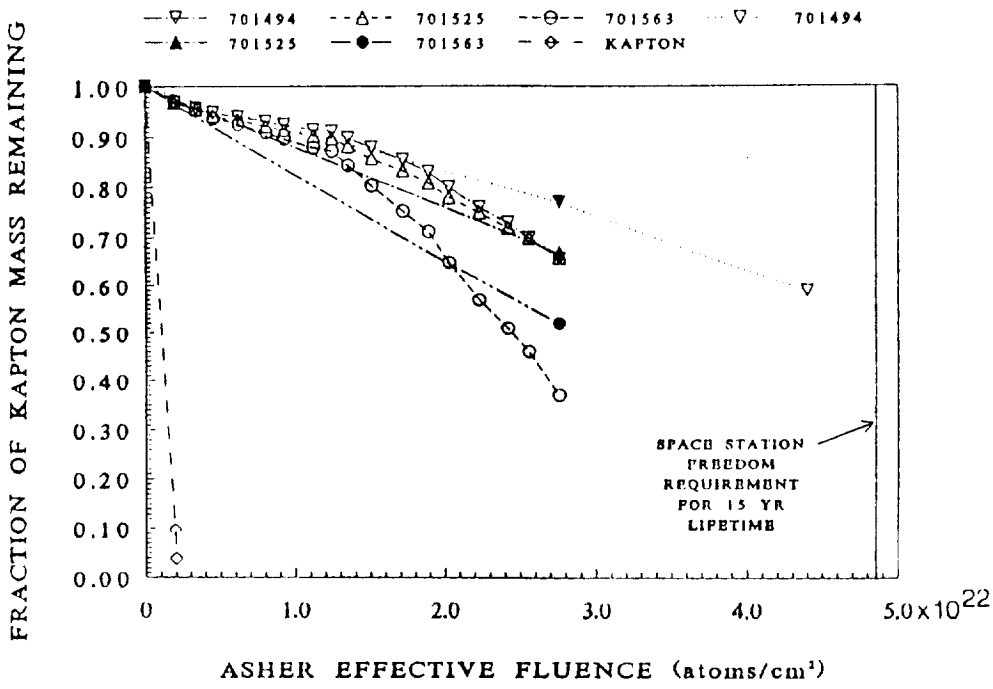

Figure 3: Mass loss for SiO_X (1300Å) coated Kapton exposed to atomic oxygen in a plasma asher.

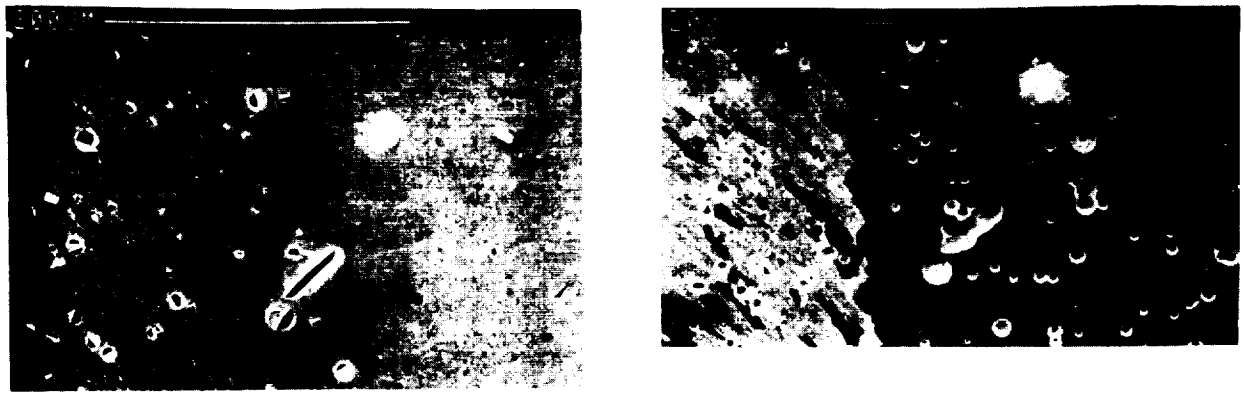

a: Prior to removal of the SiO_X coating.

b: After removal of the SiO_X coating.

Figure 4: SiO_X (590Å) coated Kapton after exposure in a plasma asher to an atomic oxygen fluence of 1×10^{21} atoms/cm^2.

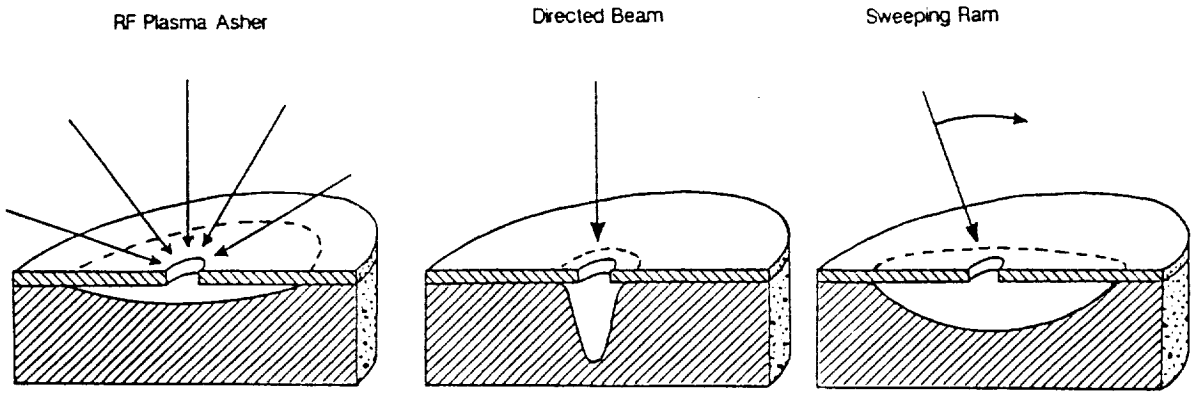

Figure 5: Atomic oxygen undercutting profiles for various directions of atomic oxygen arrival.

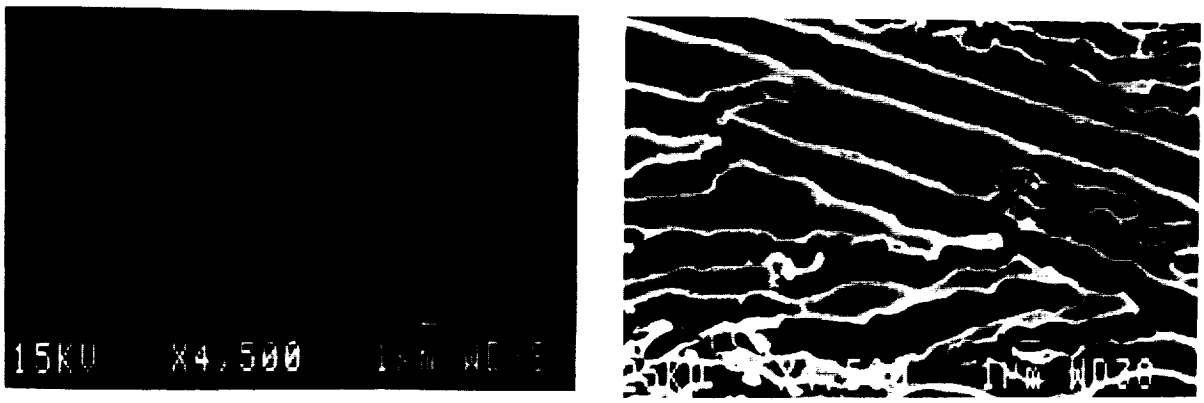

a: Prior to removal of the aluminum coating.

b: After chemical removal of the aluminum coating.

Figure 6: LDEF aluminized Kapton multilayer insulation at crack sites in the aluminization after exposure to a LEO atomic oxygen fluence of 5.77×10^{21} atoms/cm^2.

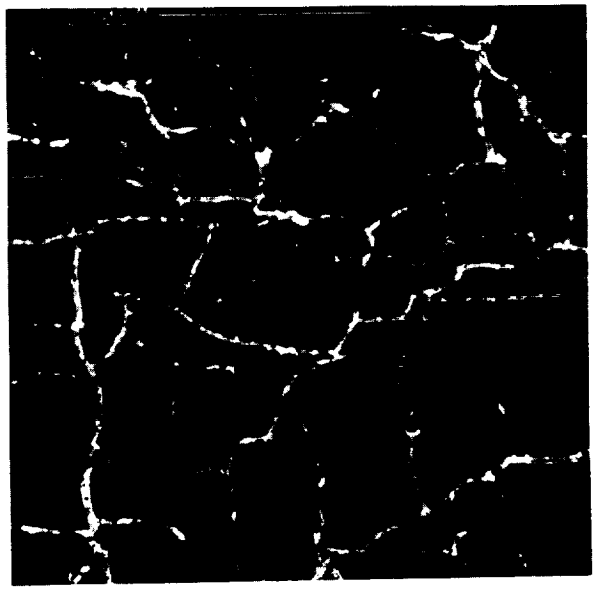

Figure 7: Silicone adhesive after LDEF exposure to an estimated fluence of 4.92×10^{21} atoms/cm^2.

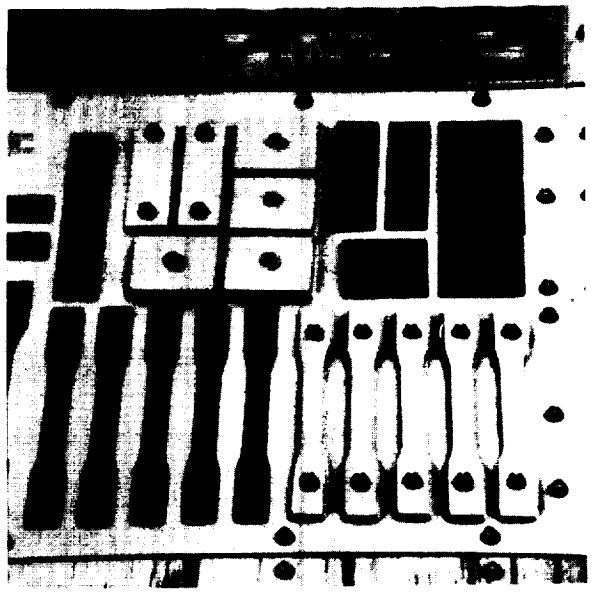

Figure 8: Photograph of LDEF silicone contamination resulting from atomic oxygen interactions with silicones.

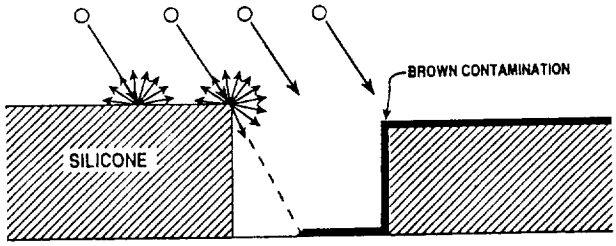

Figure 9: Atomic oxygen interactions with silicones which could produce brown contamination coatings as observed on the LDEF spacecraft.

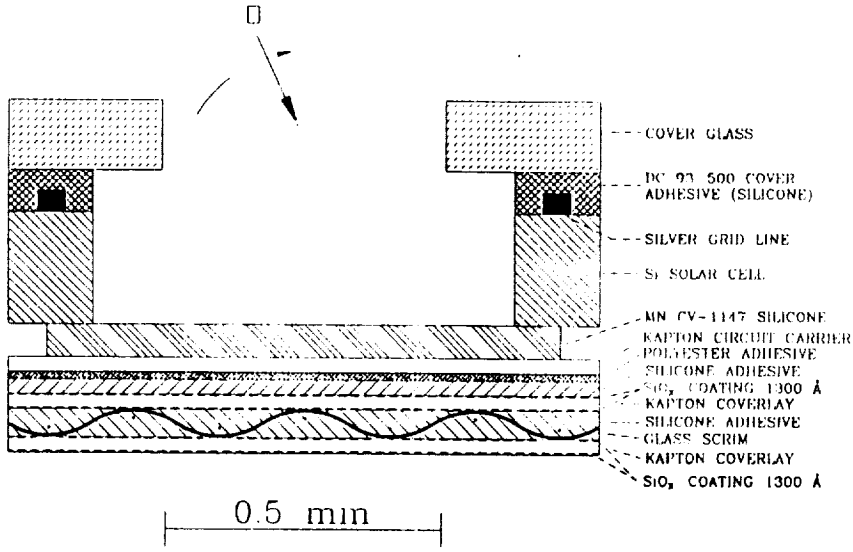

Figure 10: SSF solar array blanket cross section at the gaps between solar cells showing line of site arrival between atomic oxygen and silicone adhesive.

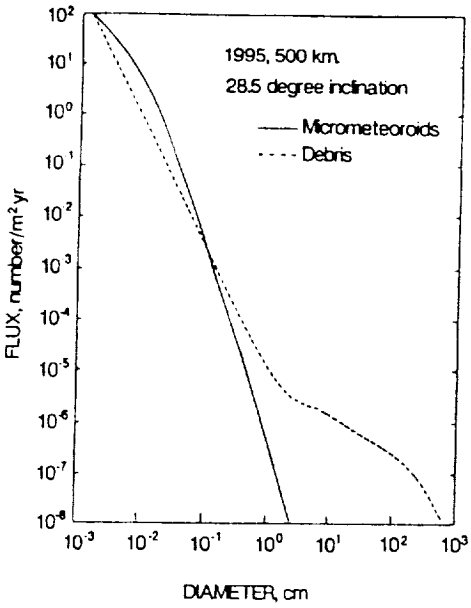

Figure 11: Micrometeoroid and debris flux for particles of equal to or smaller than a given diameter (ref. 9).

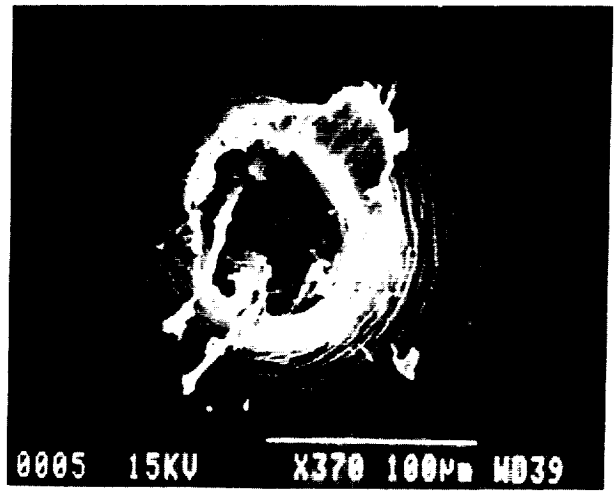

Figure 12: Debris or micrometeoroid impact site on a Kapton sample coated with 650Å of SiO_2 from the LDEF Ion Beam Textured and Coated Surfaces Experiment located at 6E.

The Space Radiation Environment for Electronics

E. G. STASSINOPOULOS AND JAMES P. RAYMOND, FELLOW, IEEE

Invited Paper

The earth's space radiation environment is described in terms of charged particles as relevant to effects on spacecraft electronics. The nature and magnitude of the trapped and transiting environments are described in terms of spatial distribution and temporal variation. The internal radiation environment of the spacecraft is described in terms of shielding the high-energy particles of the free-field environment. Exposure levels are presented in terms of ionizing radiation dose and particle fluence for comparison to electronic component susceptibility.

INTRODUCTION

The space radiation environment can have serious effects on spacecraft electronics. In this paper, the earth's space radiation environment is described in terms of trapped and nontrapped charged particles as relevant to effects on internal electronics. The nature and magnitude of the spatial distribution and temporal variation in the trapped radiation environment are presented. Transiting cosmic rays of galactic and solar origin are described, and their interaction with the earth's magnetic field is considered. In terms of spacecraft electronics, accumulated damage from electron and proton exposure will limit system endurance. Transient effects from individual high-energy protons or cosmic rays can disrupt system operation, perhaps irreversibly.

The internal radiation environment is described in terms of shielding the high-energy electrons, protons, and cosmic rays of the external environment. Exposure levels are presented in terms of ionizing radiation dose and particle fluence for comparison to electronic component damage susceptibility. Transient effects are presented in terms of particle flux for assessment of the potential frequency or probability of critical effects in the electronics. Of particular importance are the limits in shielding effectiveness for high-energy electrons, protons, and cosmic rays.

The interactions between the space radiation environment and the spacecraft electronics include those at the external surfaces as well as in the internal electronics. Important effects at the external surfaces include degradation of solar cells and charging of dielectric material, which can result in transient-producing arc-discharges. For these external effects the characterization of the free-field electron and proton environments as a function of particle energy and time are important. The internal spacecraft radiation environment is defined by particle transport through the spacecraft structure and, when necessary, shielding added to protect sensitive electronic pieceparts. Important effects on the internal electronics are performance degradation resulting from energy deposition by accumulated ionization in the semiconductor materials; accumulated atomic displacement damage in the crystal semiconductors by high-energy protons; and transient effects resulting from the ionization tracks from the interaction of a single cosmic ray or high-energy proton. Therefore, of particular interest for effects on the internal electronics are the total electron and proton exposure (i.e., fluence) and time-dependent rate of high-energy protons and cosmic rays (i.e., flux).

Manuscript received May 31, 1988; revised July 21, 1988.

E. G. Stassinopoulos is with the NASA Goddard Space Flight Center, Greenbelt, MD 20771, USA.

J. P. Raymond is with Mission Research Corporation, San Diego, CA 92123, USA.

IEEE Log Number 8824355.

I. THE TRAPPED RADIATION ENVIRONMENT

The earth's natural radiation environment consists of electrons, protons, and heavy ions: a) trapped by the earth's magnetic field, or b) transiting through the domains of the earth's artificial satellites. As the earth sweeps through the solar wind, a geomagnetic cavity is formed by the earth's magnetic field, as shown in Fig. 1, which defines the magnetosphere. The cavity is hemispherical on the sun side, with a boundary at approximately 10–12 earth radii (R_e = 6380 km). On the night side, it is cylindrical, approximately 40 R_e in diameter. Because of the sweeping action of the solar wind, it extends over several hundred R_e in the antisolar direction. The main particle trapping region, of specific interest in this paper, is the crosshatched area labeled plasmasphere.

The total magnetic field of the magnetosphere is defined in terms of two interacting and superimposed sources of internal and external origin. The internal field of the earth is thought to be caused by convective motion in the molten nickel-iron core of the planet, and by a residual permanent

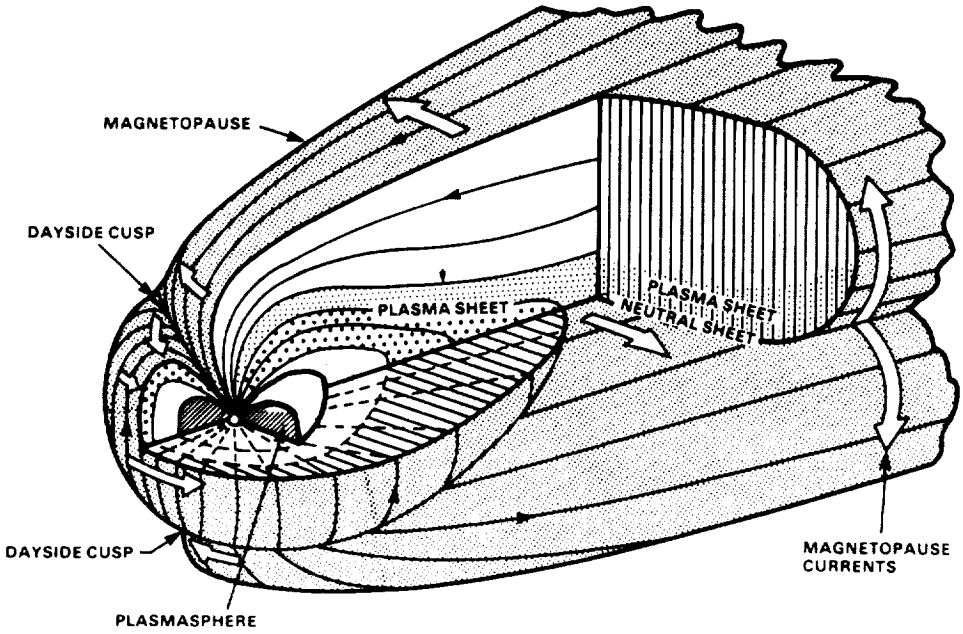

Fig. 1. Geomagnetic cavity.

magnetism in the earth's crust. The external field is comprised of the sum-total effect of currents and fields set up in the magnetosphere by the solar wind. The internal field component of the earth's magnetic field exhibits gradual changes with time, characterized as secular variations [1], [2]. These temporal effects are also observed in the shrinking value of the earth's dipole moment, and the drift in the location of the boreal (north) and austral (south) magnetic poles.

Superimposed on these slow internal changes are cyclic variations in the external field, whose magnitudes depend on the degree of perturbation experienced by the magnetosphere. Specifically, strong perturbations of the geomagnetic field are present in the outer magnetosphere, and depend on local time (diurnal effects), season (tilt effects), and solar wind conditions (including solar flares) [3]. All of these affect the magnetospheric current systems, which in turn modify the local field values.

A characteristic of the geomagnetic field, of particular significance to space radiation effects in electronics, is the Brazilian or South Atlantic Anomaly (SAA). This is primarily the result of the offset of the dipole term of the geomagnetic field by approximately 11° from the earth's axis of rotation, and displacement of about 500 km toward the Western Pacific. The effect is an apparent depression of the magnetic field over the coast of Brazil. There, the Van Allen belts reach lower altitudes, extending down into the atmosphere. The SAA is responsible for most of the trapped radiation received in low earth orbits (LEO). In contrast, on the opposite side of the globe, the Southeast-Asian Anomaly displays correspondingly stronger field values, and the trapped particle belts are located at higher altitudes.

A. Trapped Radiation Domains

The earth's magnetic field, above the dense atmosphere, is populated with trapped electrons, protons, and small amounts of low energy heavy ions. These particles gyrate around and bounce along magnetic field lines, and are reflected back and forth between pairs of conjugate mirror points (i.e., regions of maximum magnetic field strength along their trajectories) in opposite hemispheres. At the same time, because of their charge, electrons drift eastward around the earth, while protons and heavy ions drift westward. Fig. 2 [4] illustrates the spiral, bounce, and drift motion of the trapped particles.

The magnetosphere can be divided into five domains for particle species populating or visiting, as shown in Fig. 3. The strong dependence of trapped particle fluxes on altitude and latitude is expressed in terms of the McIlwain L parameter [5], where L is a dimensionless ratio of the earth's radius, approximately equal to the geocentric distance of a field line in the geomagnetic equator. Also shown in Fig. 3 are the domains mapped by using the dipole field equation

$$R = L \cos^2 \Lambda$$

(or $R - \Lambda$ space). R is defined as the radial distance, and Λ is defined as the invariant latitude. It should be noted that the representation using L becomes increasingly invalid for equatorial distances greater than four times R_e because of the more complex particle motion in the geomagnetic field, and the distortion of the geomagnetic cavity by solar wind interaction effects.

The indicated domain boundaries should be considered only transitions, not actual lines. These boundaries are assumed for modeling purposes and, additionally, are used here for a qualitative picture of the charged particle distribution. "Real" boundaries are diffused areas, varying with particle energy, and fluctuating in position due to magnetic perturbations, local time effects, solar cycle variations (minimum and maximum activity phases), and individual solar events.

1) Electrons: Energetic Van Allen belt electrons are distinguished into "inner zone" and "outer zone" popula-

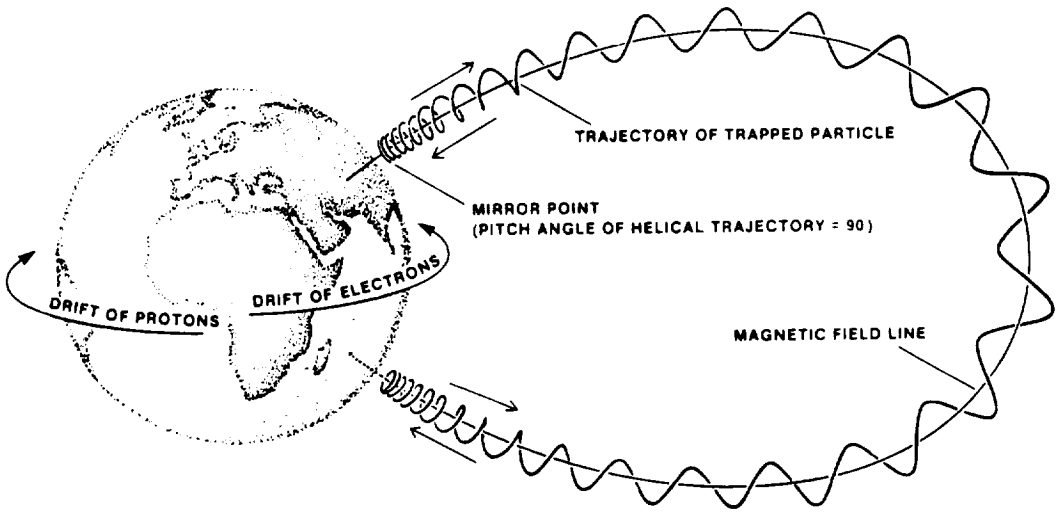

Fig. 2. Motions of trapped particles.

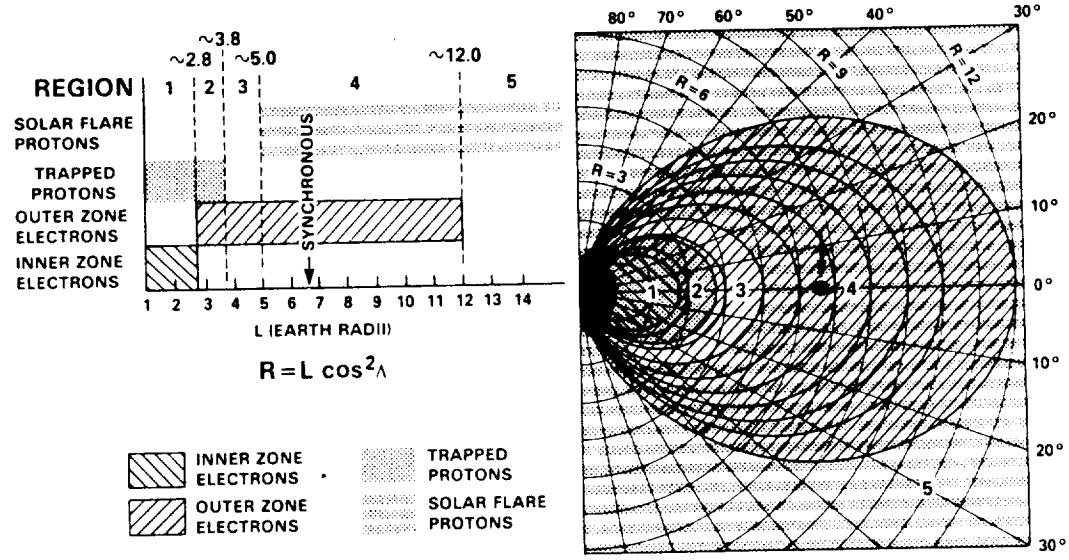

Fig. 3. Charged particle distribution in the magnetosphere.

tions. The volume of space occupied by the "inner zone" extends at the equator to about 2.4 R_e. These domains are indicated, respectively, by regions 1, and 2-3-4 in Fig. 3. The L = 2.8 line is used to separate the inner and outer zone domains, while the termination of the outer zone at L = 12 is intended only to delineate the maximum outward extent of stable, or pseudo-electron trapping. The region between L = 2.5 and 2.8 is called the "slot." During magnetospherically quiet times, its electron density is very low. However, during magnetic storms, the electron flux in the "slot" may increase by several orders of magnitude.

The inner zone electrons are less severe compared to the outer zone electrons. Specifically, the outer zone has peak fluxes exceeding those of the inner zone by about an order of magnitude. Also, the outer zone spectra extend to much higher energies (~7 MeV) than the inner zone spectra (<5 MeV). In this paper, we will present a detailed description of both the external and internal radiation environments for low earth orbits (i.e., LEO) in the inner zone, and for geostationary orbits (i.e., GEO) within the outer zone.

2) Protons: Protons with energies greater than 10 MeV populate regions 1 and 2 with an approximate trapping boundary placed at L = 3.8 as shown Fig. 3. In contrast to the electrons, the energetic trapped protons (E > 1 MeV) occupy a volume of space which varies inversely and monotonically with their energy as shown in Fig. 4. Consequently, these particles cannot be assigned to "inner" and "outer" zones. Fig. 5 shows the proton flux intensities as a function of radial distance and energy. In low earth orbits, the most intense and penetrating radiation is encountered in the form of protons in the South Atlantic Anomaly (SAA).

B. Models

Available radiation measurements from space form the basis for models of the trapped electron and proton envi-

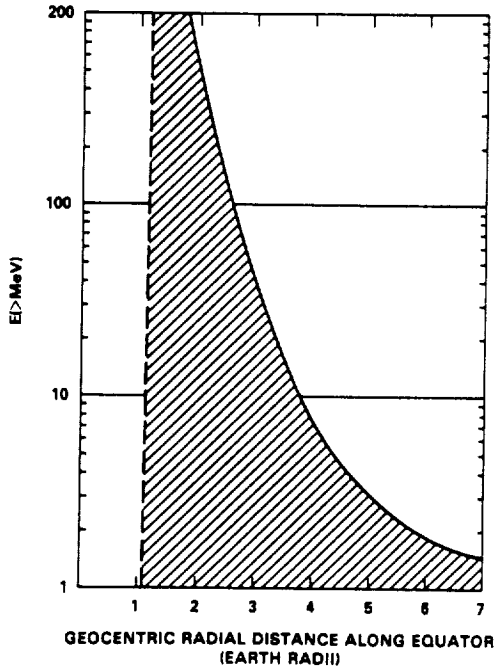

Fig. 4. Trapped proton population as a function of energy.

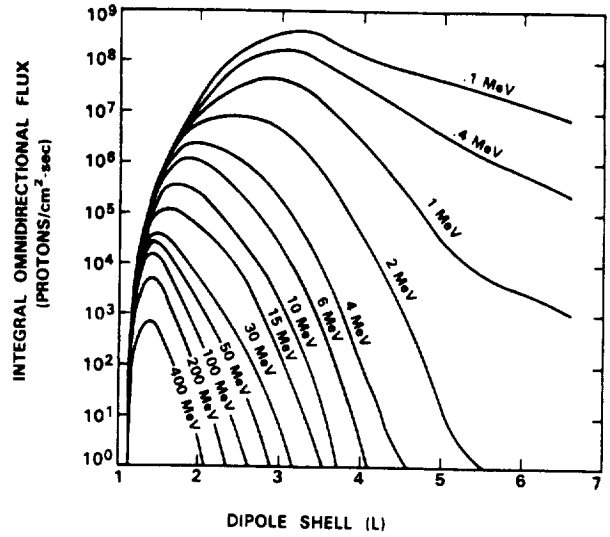

Fig. 5. Equatorial radial profiles for proton fluxes.

ronment. These models have been developed by the U.S. National Space Science Data Center (NSSDC) at NASA's Goddard Space Flight Center. All models are constructed with several dozen data sets from a corresponding number of satellites, providing a wide spatial and a long temporal coverage.

The most recent of these models, AP8 for protons [6] and AE8 for electrons [7], permit long term average predictions of trapped particle fluxes encountered in any orbit, and currently constitute the best estimates for the trapped radiation belts. However, statistics associated with randon fluctuations and short-term cyclical variations have been averaged out. The solar cycle dependence is reflected by the average conditions for the solar minimum and solar maximum activity phases of the 11-year cycle.

The predictions of these models for low earth orbit missions are presented in Tables 1 and 2 and Figs. 6 and 7. Table 1 presents the averaged orbit integrated fluxes for protons as a function of energy, parametrically for orbital inclinations of 28.5°, 60°, and 90°, all for both 300 km and 500 km circular orbit altitudes. Table 2 presents comparable data for the trapped electron environment. Fig. 6 gives the integral proton spectra for a circular 500 km, 60° inclination

Table 1 Trapped Proton Fluxes, LEO, Solar Minimum

E(>MEV)	300 KM INCLINATION			500 KM INCLINATION		
	28.5 DEG	60 DEG	90 DEG	28.5 DEG	60 DEG	90 DEG
0.04	5.420E+05	3.038E+08	1.509E+08	6.730E+06	9.595E+08	5.013E+08
0.07	5.399E+05	2.577E+08	1.297E+08	6.714E+06	7.947E+08	4.176E+08
0.10	5.379E+05	2.198E+08	1.121E+08	6.699E+06	6.620E+08	3.512E+08
0.50	5.202E+05	5.145E+07	3.055E+07	6.550E+06	1.329E+08	8.003E+07
1.00	5.028E+05	2.056E+07	1.386E+07	6.411E+06	5.126E+07	3.384E+07
2.00	4.945E+05	8.707E+06	6.445E+06	6.305E+06	2.246E+07	1.598E+07
3.00	4.890E+05	5.687E+06	4.265E+06	6.208E+06	1.539E+07	1.124E+07
4.00	4.835E+05	3.895E+06	2.949E+06	6.113E+06	1.123E+07	8.390E+06
5.00	4.781E+05	2.792E+06	2.129E+06	6.020E+06	8.679E+06	6.606E+06
6.00	4.728E+05	2.092E+06	1.606E+06	5.929E+06	7.054E+06	5.453E+06
8.00	4.613E+05	1.535E+06	1.184E+06	5.739E+06	5.663E+06	4.448E+06
10.00	4.501E+05	1.191E+06	9.242E+05	5.556E+06	4.774E+06	3.795E+06
15.00	4.348E+05	9.010E+05	7.073E+05	5.234E+06	3.947E+06	3.169E+06
20.00	4.203E+05	7.359E+05	5.827E+05	4.936E+06	3.422E+06	2.760E+06
25.00	4.064E+05	6.609E+05	5.241E+05	4.720E+06	3.169E+06	2.556E+06
30.00	3.930E+05	6.026E+05	4.779E+05	4.517E+06	2.958E+06	2.384E+06
35.00	3.770E+05	5.588E+05	4.433E+05	4.313E+06	2.780E+06	2.248E+06
40.00	3.616E+05	5.201E+05	4.129E+05	4.119E+06	2.617E+06	2.123E+06
45.00	3.470E+05	4.857E+05	3.857E+05	3.935E+06	2.468E+06	2.009E+06
50.00	3.331E+05	4.548E+05	3.613E+05	3.761E+06	2.330E+06	1.902E+06
60.00	2.999E+05	3.917E+05	3.118E+05	3.382E+06	2.055E+06	1.681E+06
80.00	2.441E+05	2.959E+05	2.363E+05	2.748E+06	1.613E+06	1.324E+06
100.00	1.997E+05	2.276E+05	1.823E+05	2.243E+06	1.279E+06	1.053E+06
150.00	1.018E+05	1.055E+05	8.646E+04	1.279E+06	6.951E+05	5.742E+05
200.00	5.303E+04	5.103E+04	4.278E+04	7.439E+05	3.896E+05	3.226E+05
250.00	2.684E+04	2.526E+04	2.144E+04	4.334E+05	2.246E+05	1.856E+05
300.00	1.377E+04	1.281E+04	1.100E+04	2.547E+05	1.313E+05	1.082E+05
350.00	6.940E+03	6.559E+03	5.680E+03	1.506E+05	7.733E+04	6.359E+04
400.00	3.219E+03	3.139E+03	2.714E+03	8.914E+04	4.594E+04	3.753E+04
500.00	4.961E+02	7.257E+02	5.937E+02	3.108E+04	1.618E+04	1.328E+04

Table 2 Trapped Electron Fluxes, LEO, Solar Minimum

E(>MEV)	300 KM INCLINATION			500 KM INCLINATION		
	28.5 DEG	60 DEG	90 DEG	28.5 DEG	60 DEG	90 DEG
0.04	2.973E+08	3.203E+09	2.971E+09	5.153E+09	9.171E+09	7.876E+09
0.07	2.351E+08	2.391E+09	2.257E+09	4.082E+09	7.007E+09	6.066E+09
0.10	1.861E+08	1.795E+09	1.730E+09	3.236E+09	5.382E+09	4.712E+09
0.20	5.629E+07	6.779E+08	7.424E+08	9.975E+08	1.908E+09	1.816E+09
0.30	2.227E+07	3.631E+08	4.262E+08	3.969E+08	9.484E+08	9.514E+08
0.40	1.144E+07	2.384E+08	2.849E+08	2.017E+08	5.895E+08	6.029E+08
0.50	5.897E+06	1.616E+08	1.950E+08	1.030E+08	3.807E+08	3.944E+08
0.60	3.985E+06	1.283E+08	1.526E+08	6.850E+07	2.917E+08	3.007E+08
0.70	2.701E+06	1.027E+08	1.204E+08	4.574E+07	2.258E+08	2.315E+08
0.80	1.948E+06	8.399E+07	9.744E+07	3.268E+07	1.813E+08	1.845E+08
0.90	1.494E+06	7.001E+07	8.051E+07	2.494E+07	1.504E+08	1.515E+08
1.00	1.147E+06	5.850E+07	6.669E+07	1.904E+07	1.252E+08	1.248E+08
1.25	7.213E+05	3.857E+07	4.262E+07	1.179E+07	8.119E+07	7.931E+07
1.50	4.549E+05	2.554E+07	2.742E+07	7.310E+06	5.292E+07	5.076E+07
1.75	3.051E+05	1.747E+07	1.828E+07	4.870E+06	3.561E+07	3.371E+07
2.00	2.053E+05	1.199E+07	1.224E+07	3.250E+06	2.407E+07	2.250E+07
2.25	1.392E+05	8.275E+06	8.289E+06	2.194E+06	1.644E+07	1.516E+07
2.50	9.419E+04	5.725E+06	5.637E+06	1.484E+06	1.127E+07	1.026E+07
2.75	3.788E+04	3.899E+06	3.751E+06	5.934E+05	7.373E+06	6.610E+06
3.00	1.521E+04	2.695E+06	2.529E+06	2.405E+05	4.956E+06	4.361E+06
3.25	4.850E+03	1.856E+06	1.695E+06	7.591E+04	3.324E+06	2.862E+06
3.50	1.357E+03	1.292E+06	1.148E+06	2.394E+04	2.274E+06	1.914E+06
3.75	3.874E+02	8.495E+05	7.316E+05	7.263E+03	1.474E+06	1.206E+06
4.00	0.000E+00	5.650E+05	4.726E+05	8.860E+02	9.693E+05	7.712E+05
4.50	0.000E+00	2.066E+05	1.643E+05	0.000E+00	3.493E+05	2.633E+05
5.00	0.000E+00	6.828E+04	5.129E+04	0.000E+00	1.143E+05	7.979E+04
5.50	0.000E+00	1.572E+04	1.188E+04	0.000E+00	2.659E+04	1.751E+04
6.00	0.000E+00	2.858E+03	1.970E+03	0.000E+00	3.923E+03	2.470E+03
6.50	0.000E+00	0.000E+00	0.000E+00	0.000E+00	1.235E+02	6.052E+01
7.00	0.000E+00	0.000E+00	0.000E+00	0.000E+00	0.000E+00	0.000E+00

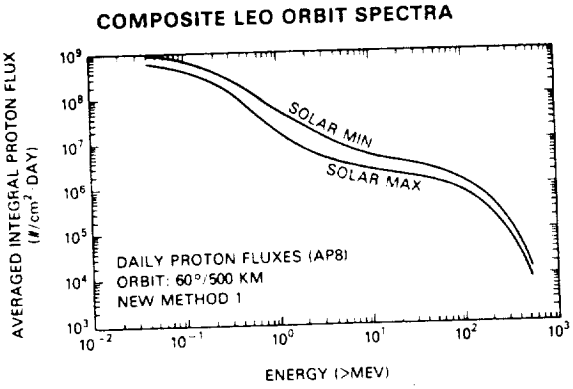

Fig. 6. Low earth orbit (LEO) proton fluxes.

orbit, for both solar minimum and solar maximum conditions. The relative hardness of the LEO proton spectrum should be noted. Between 50 and 500 MeV the proton flux decreases only by a factor of 4. Fig. 7 presents the comparable data for the trapped electron environment.

It should be noted that the model in the low altitude regime (< 1000 km), that is, in the atmospheric cutoff region, must be related to the correct geomagnetic field strength. If used with current or projected (i.e., future) field strength values, the predicted fluxes will be too high by factors ranging from approximately 2 (at 800–1000 km) to approximately 50 (at 200–500 km). This is the result of the geomagnetic field changing with time. In this process, the dipole moment is decreasing, pulling heavily populated field lines down into the denser regions of the atmosphere, where there occur

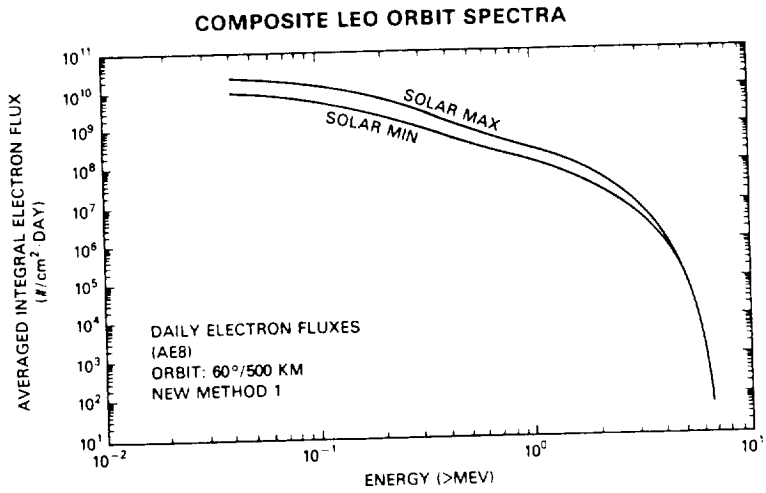

Fig. 7. Low earth orbit (LEO) electron fluxes.

significant particle losses (mostly due to coulomb scattering), which are not represented in the model.

The geosynchronous integral electron spectrum, obtained from the AE8-MAX model, is given in Table 3 and is plotted in Fig. 8. Worst and best cases are shown, corresponding to "parking" longitudes at 160° W (L = 7.0), and 70° W (L = 6.6), respectively. The flux ratio between the worst and best cases is about 1.8 for electron energies greater than 1 MeV, and 2.3 for electron energies greater than 2 MeV.

The proton spectrum at GEO, in contrast to that of LEO, is very soft and, essentially, is depleted for protons of energies greater than 1.75 MeV. Thus, trapped protons in GEO are stopped by very small material thicknesses (approximately 0.05 mm of aluminum), and are not of concern to the internal electronics.

Table 3 Geostationary Electron Fluxes

E(>MEV)	70 DEG W	160 DEG W
0.04	3.775E+07	4.643E+07
0.07	3.023E+07	3.847E+07
0.10	2.421E+07	3.188E+07
0.20	1.145E+07	1.587E+07
0.30	5.944E+06	8.575E+06
0.40	3.383E+06	5.044E+06
0.50	1.925E+06	2.967E+06
0.60	1.224E+06	2.048E+06
0.70	7.788E+05	1.414E+06
0.80	5.290E+05	9.879E+05
0.90	3.838E+05	6.983E+05
1.00	2.784E+05	4.935E+05
1.25	1.338E+05	2.475E+05
1.50	6.435E+04	1.242E+05
1.75	3.497E+04	7.171E+04
2.00	1.900E+04	4.142E+04
2.25	9.313E+03	2.128E+04
2.50	4.653E+03	1.093E+04
2.75	2.816E+03	6.494E+03
3.00	1.737E+03	3.858E+03
3.25	1.118E+03	2.484E+03
3.50	7.196E+02	1.600E+03
3.75	4.260E+02	8.527E+02
4.00	2.522E+02	4.546E+02
4.50	6.825E+01	1.187E+02
5.00	1.673E+00	4.519E+00
5.50	0.000E+00	0.000E+00
6.00	0.000E+00	0.000E+00
6.50	0.000E+00	0.000E+00
7.00	0.000E+00	0.000E+00

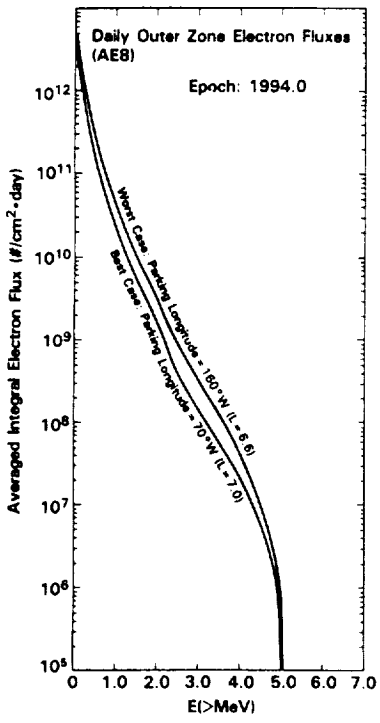

Fig. 8. Geostationary electron spectra.

C. *Variations*

The trapped particle fluxes respond to changes in the geomagnetic field induced by solar activity, and, therefore, exhibit a strong dynamic behavior, especially in the outer belts. Satellite measurements in geosynchronous (GEO) equatorial orbits have revealed a complicated temporal pattern consisting of a superposition of several cyclical variations in conjunction with sporadic fluctuations [8]–[10]. The main periodic variations include a diurnal cycle, which in GEO is characterized by order-of-magnitude electron flux changes [8], and the 11-year solar activity cycle.

Sporadic magnetic storms in GEO can produce a modulation of the electron flux above 50 keV by an order of magnitude within a period of less than 10 minutes [9], and with a corresponding decay in days. Substorms, which are a common feature of the midnight to dawn sector of a GEO orbit, result in the injection of electrons with energies between 50 and 150 keV from the magnetospheric tail region. The electron flux above 200 keV remains constant, or actually decreases. The short term variations in electron flux in the outer belt, including local time variations, are particularly critical in the assessment of spacecraft charging effects. For the internal electronics, the principal effect of the electron exposure is ionization damage, which accumulates slowly over the life of the mission.

Another important solar-activity-induced modulation of the trapped particle population, particularly of protons, occurs in the low altitude regime of the magnetosphere. Here, during the active phase of the solar cycle, the increased energy output from the sun causes the atmosphere to expand, thereby raising the density of the atmospheric constituents normally encountered at heights between 200 and 1000 km. This increase in atmospheric density depletes, through coulomb scattering, the populations of those trapped particles that have their mirror points at these low altitudes, with significant effects on the radiation exposure of satellites orbiting in that domain.

The solar cycle variations observed in some areas of the trapped particle domain are functions of energy and magnetic parameter L. They generally have opposite effects on each particle specie, particularly in the low altitude regime:

	Solar Min	Solar Max
Electron Intensities	lower	higher
Proton Intensities	higher	lower

No solar cycle changes of consequence have been measured in the heart of the proton trapping domain. No significant long term variations, within current models, occur in the electron populations at geostationary altitudes. However, in the atmospheric cutoff regions, electron and proton variations may range up to a factor of 5.

D. Flux-Free Time

As mentioned previously, the South Atlantic Anomaly (SAA) is a region of trapped particle radiation close to the earth. Hence, for low altitude, low inclination orbits, the SAA is the most important factor in determining the level of radiation exposure of spacecraft. For low earth orbits (LEO) with higher inclinations (> 35°, the protrusions of the outer zone electron belts (the electron "horns") in the mid-latitude regions must also be considered. Of particular importance is the temporal distribution of the proton exposure, which determines the maximum rate of potential proton-induced single-event upsets in the electronics, as well as the periods in which no upsets will be observed.

The intermittent exposure of LEO satellites to the trapped Van Allen belt radiation is illustrated for electrons in Fig. 9 for a circular 900 km, 99° inclination orbit during its worst pass through the SAA. Note in Fig. 9 that even in a worst case pass, there are time periods during which instantaneous electron fluxes above 0.5 MeV are below 1 particle per square centimeter per second. The same is true for protons above 5 MeV. These time periods are the "flux free time" (FFT) intervals. They may occur over short orbit segments (partial FFT per period), or over the entire length of a revolution (total FFT per period). In terms of geomagnetic geometry, the FFTs establish the duration for which the trajectory lies outside the trapping domain of the corresponding particle species, evaluated at the given energies. Or, conversely, they are a measure of the degree to which the trajectory is exposed to the charged particle trapping domains.

The number of consecutive flux-free orbits of circular trajectories is primarily a function of altitude and inclination and, to a lesser degree, a function of particle energy. Generally, higher energies will yield longer FFTs because the more energetic particles occupy a smaller volume of space, particularly in the case of protons. For an orbit configuration similar to the one illustrated in Fig. 9, and for protons with energies greater than 5 MeV, or electrons of energy greater than 0.5 MeV, there are no completely flux-free orbits. The total FFT is entirely composed of contributions from partially exposed revolutions. In terms of the solar cycle, it can be summarized in percent of total mission duration as:

	Protons	Electrons
	(E > 5 MeV)	(E > 0.5 MeV)
Solar Minimum	81%	33%
Solar Maximum	83%	53%

For a 500 km, 30° inclination LEO, the FFT includes six completely flux free orbits per day, that is, orbits which do not pass through the SAA or the electron "horn" regions. In this case, the FFT can be summarized in percent of total mission duration as:

	Protons	Electrons
	(E > 5 MeV)	(E > 0.5 MeV)
Solar Minimum	90%	89%
Solar Maximum	92%	88%

In terms of the spacecraft electronics, the fluxes of the electron and proton environments are important in the total ionizing radiation induced damage, and the proton flux and flux-free-time are important in the potential rate of proton-induced transient upsets.

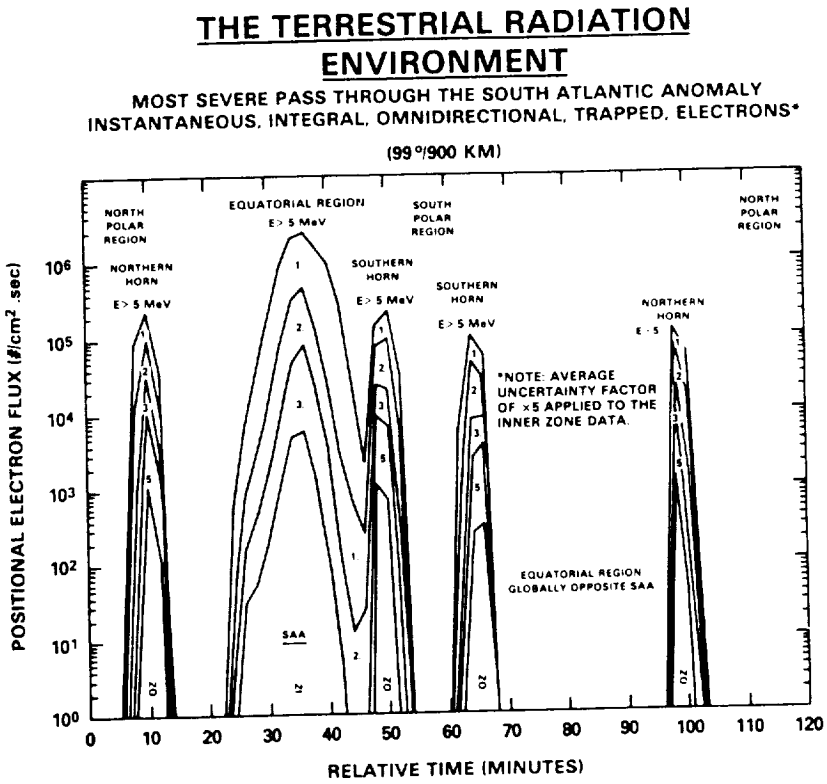

Fig. 9. Positional electron flux profile.

E. Artificial Enhancement

A severe hazard for space missions could be introduced by a high altitude nuclear explosion. Such an effect would result in the injection into the magnetosphere of energetic electrons from the beta decay of fission fragments. Subsequent trapping of the electrons in the magnetic field [11] could produce an enhancement of the electron population by many orders of magnitude.

The principal hazard would be to missions in low earth orbits, mainly because of an expected very stable trapping with lifetimes up to eight years [11]. Fig. 10 shows the isochronal contours for the trapped electrons resulting from the STARFISH exoatmospheric nuclear explosion of July 1962 over Johnston Island in the Pacific. However, depending on the location of the explosion, the injection could also produce a temporary large enhancement of the electron environment at geostationary orbits. At GEO, the trapping would be less stable, with exponential decay periods of between 10 and 20 days. The apparent longevity, or conversely, the decay rate, of such fission electrons depends to a large extent on the injection latitude and altitude; that is, it is a function of the magnetic dipole shell parameter L and, to a lesser degree, of magnetic field strength [12].

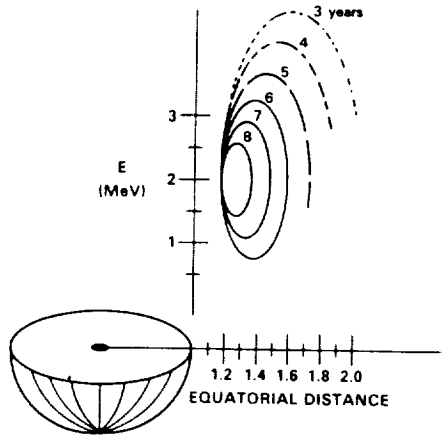

Fig. 10. Isochronal contours for STARFISH electron longevity.

For the internal electronics, it is important to note that both the total ionizing exposure level and exposure dose rate are substantially increased by the artificially enhanced environment.

II. Trapped Radiation Transport, Shielding, and Doses

A. Emerging Radiation

In interacting with spacecraft materials, the electrons and protons of the trapped radiation belts are modified in intensity by shielding, and modified in character through the production of secondary radiation. The secondary radiation can extend the penetration of the primary radiation and lead to an increase in dose deposition over that of the attenuated incident radiation. The most significant secondary radiation is the bremsstrahlung, or "braking radiation," produced in the deceleration of electrons penetrating the spacecraft. This is a continuous X-ray spectrum emitted roughly in the direction of electron penetration. The mean X-ray energy is about one-third that of the initial electron energy. The bremsstrahlung intensity depends linearly on the atomic number of the spacecraft material and on the square of the initial electron energy. Bremsstrahlung from energetic electrons populating the radiation belts is very penetrating, and thus difficult to attenuate, especially with the low-atomic number materials popular on spacecraft (e.g., aluminum). On the other hand, these low-atomic number materials tend to produce less bremsstrahlung.

1) Electrons and Bremsstrahlung: To illustrate, Figs. 11 and 12 show the emerging electron and bremsstrahlung spectra behind spherical aluminum shielding for the incident environment of a 500 km circular orbit of 60° inclination. As the curves of Fig. 11 clearly indicate, the trapped electrons are very effectively attenuated by the aluminum

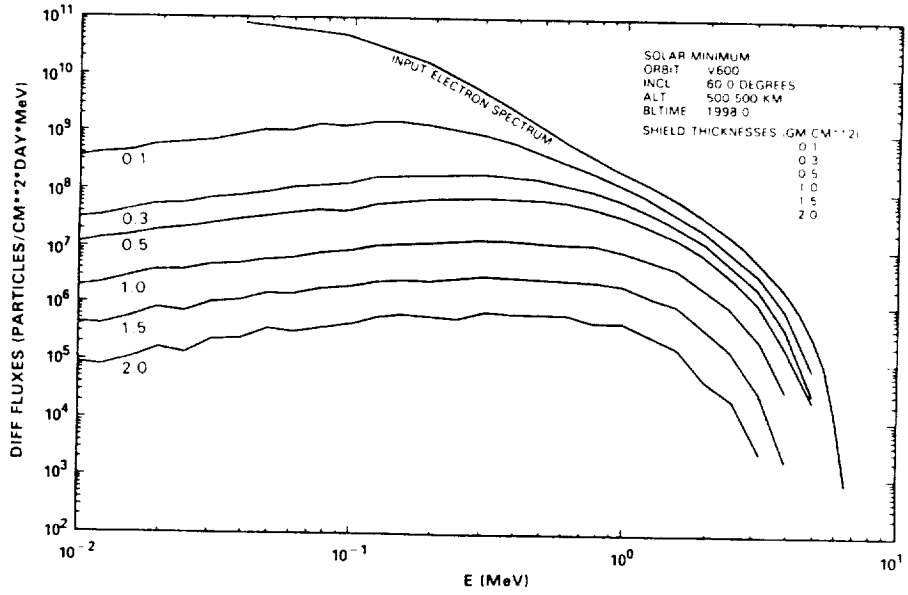

Fig. 11. Emerging electron spectra behind spherical aluminum shields.

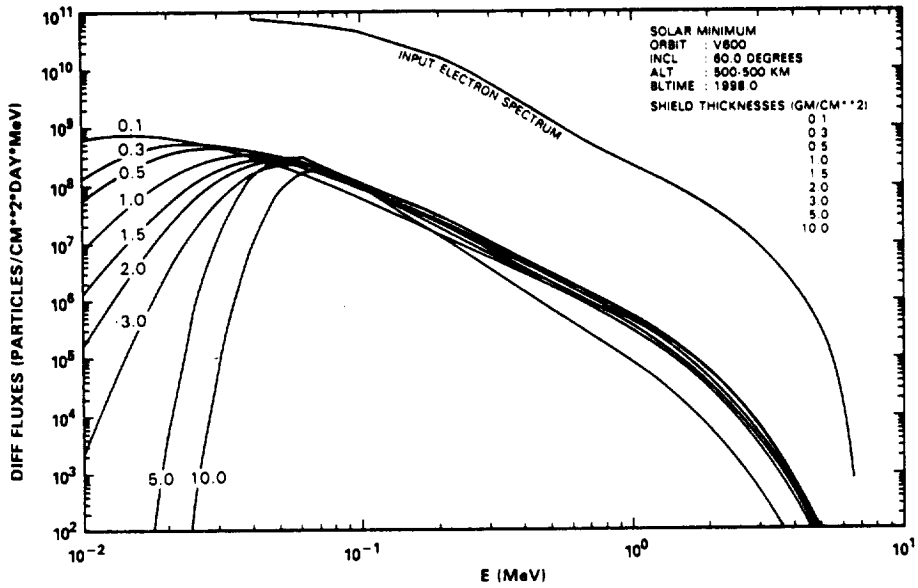

Fig. 12. Emerging bremsstrahlung spectra behind spherical aluminum shields.

shield, and are nearly all stopped by thickness greater than 2 grams per square centimeter, even at the highest electron energies. However, as shown in Fig. 12, the bremsstrahlung flux levels for energies above 40 keV are not significantly affected by any of the aluminum shields from 0.1 to 10 grams per square centimeter. It is important to note, however, that above 100 keV, the photon fluxes are, on the average, over three orders of magnitude lower than the incident electron flux at corresponding energy levels.

2) Trapped Protons: Transport of the trapped protons is illustrated in Fig. 13, which shows the emerging proton spectra behind spherical aluminum shields for the 500 km circular, 60° inclination orbit. As shown, the aluminum shielding is very effective for the low energy protons, but ineffective for the high energy (greater than 30 MeV) protons. The shielding effectiveness of the low proton energies is important in reducing the ionizing energy deposition in the internal electronics. On the other hand, the "hardening" of the proton spectra provides little help in reducing potential proton-induced single-event upsets.

3) Variables Affecting Dose Evaluations: Obtaining estimates of the dose on a given component of the internal electronics in a spacecraft is a complex process involving several variables that directly affect the results. These variables include: 1) primary environment definition, 2) description of the input spectra, and 3) contributions from secondary particles and photons.

Four areas stand out that are of particular concern to shielding and transport evaluations. These are completely independent from, and unrelated to, the definition of the

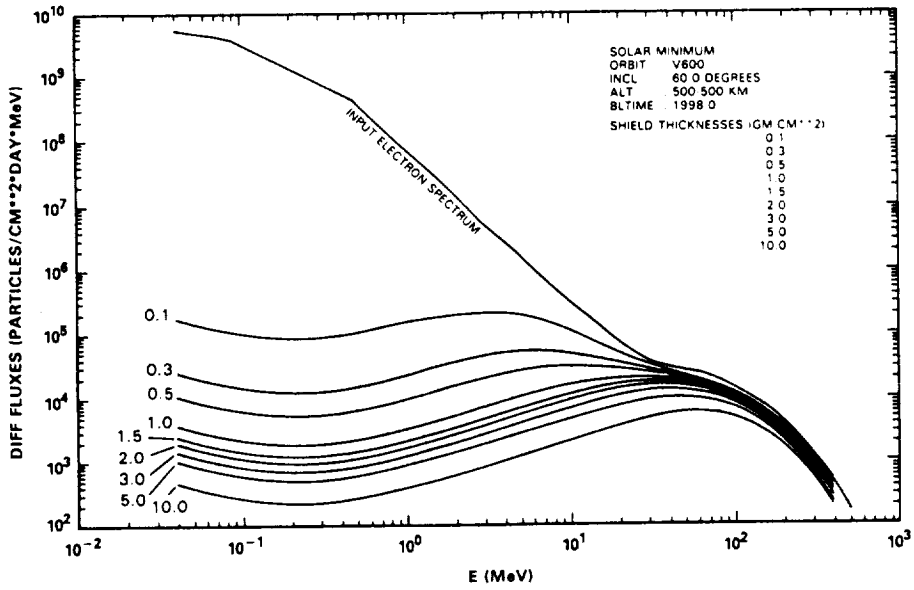

Fig. 13. Emerging trapped proton spectra behind spherical aluminum shields.

spacecraft-encountered radiation environment. The areas are: 1) shield geometry and shielding analysis technique, b) shield material composition, c) target (i.e., component) composition (e.g., package, passivation, metalization and semiconductor of a complex microcircuit), and d) dose units. Each of these, as shown in Table 4, offers a multiplicity

Table 4 Areas of Concern for Shielding and Transport Evaluation

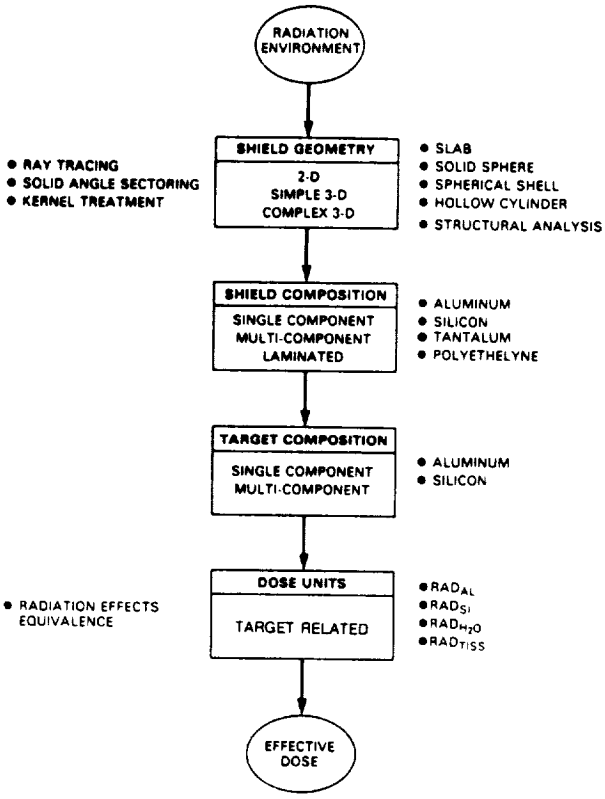

of choices and conditions that need to be clearly identified and defined whenever calculations are performed and results presented. Otherwise, the comparison of dose data compiled by several independent sources, although derived from the same spacecraft surface incident spectrum, becomes meaningless and futile. In such cases, disagreements by factors up to 20 have been known to occur.

Energy deposition in the internal electronics is measured in units of rads (material). A rad (radiation absorbed dose) is defined as 100 ergs of energy deposition per gram of absorber material, without reference to the nature of the energy deposition. The MKS equivalent of the rad is the Gray, which is defined as the energy deposition of 1 Joule in one kg of material (e.g., 100 rad(Al) = 1 Gy(Al)). For electron exposure, the energy deposition is almost all by ionization. For proton exposure, the energy deposition includes both ionization and atomic displacements.

The calculation of radiation penetration and dose deposition, in principle, is well understood (with the possible exception of intra-nuclear cascades), and usually can be carried out to adequate accuracy with a variety of available radiation transport codes. Analysis of the internal secondary radiation environment in specific spacecraft, while complex, is possible, and has been performed using ray tracing techniques, solid angle sectoring, and Monte Carlo modeling [13].

Generally, space radiation transport and dose calculations use idealized shielding configurations such as solid or hollow spheres, semi-infinite slabs, and cylinders, usually with aluminum as a reference material. The use of the idealized configurations readily permits parametric analysis of dose attenuation, exploration of the consequences of environmental uncertainties, and identification of the shielding required for a given spacecraft. In comparing results from different geometries, it should be noted that for omnidirectional isotropic flux incidence, spherical shields yield dose results roughly 2 to 6 times higher than 4π exposure of slab shields with centered dose points. Cylindrical shields yield intermediate results between the spherical and slab configurations. The differences in configurations, however, also depend on particle species, energy spectrum, shield thickness, and (particularly) target composition.

B. Ionizing Radiation Dose

To illustrate the ionizing dose exposure, daily dose values for low earth orbits (LEO) and geostationary orbits (GEO) are presented in Tables 5 through 7 and Figs. 14 through 16. The materially attenuated doses and fluxes presented were calculated with state-of-the-art transport codes [13], [14].

Tables 5 through 7 present the calculated daily doses for LEO at 500 km altitudes and inclinations of 28.5, 60, and 90 degrees for solar minimum conditions based on the trapped electron and proton models. Daily silicon doses in LEO at 500 km altitude and 30° inclination for solar minimum and maximum, are shown in Fig. 14 for a two-sides exposure of aluminum slab shields and for a solid spherical shield, as an average over 15 orbits. The electron dose includes the bremsstrahlung contribution.

As discussed previously, the South Atlantic Anomaly (SAA) is the primary contributor to the doses accumulated by spacecraft in LEO. Fig. 15 shows contours of total dose for an attitude of 500 km for a spherical shield thickness of 2 grams per square centimeter of aluminum. Superimposed on the world maps are the worst case passes through the SAA for 28.5, 57, and 90 degree inclination orbits. As mentioned previously, for low inclination orbits ($<45°$), there are periods when complete revolutions are in flux free time. These time periods are especially important when considering extra-vehicular-activities (EVAs).

The corresponding electron-plus-bremsstrahlung daily dose for an aluminum shield of solid sphere geometry in GEO at the parking longitude, with the lowest average flux (70° W), is illustrated in Fig. 16 in the form of a dose-depth curve. For the parking longitude with the large average flux (160° W), the dose behind a 2 gram per square centimeter shielding thickness is a factor of about 1.7 higher, regardless of geometry.

C. Permanent Damage Susceptibility of Electronics

The basic permanent damage mechanisms in semiconductor devices exposed to high-energy electrons and protons are accumulated ionization effects and atomic displacements in bulk semiconductors. Energy deposition

Table 5 Daily Dose, 28.5 Degrees/500 km, Solar Minimum

S GM/SQCM	T MM	T MILS	ELEC RADS-AL	BREM RADS-AL	PROTON RADS-AL	TOTAL RADS-AL
0.01	0.04	1.00	2.494E+02	9.518E-02	1.805E+00	2.513E+02
0.02	0.07	3.00	1.417E+02	6.745E-02	1.629E+00	1.434E+02
0.03	0.11	4.00	8.896E+01	5.151E-02	1.540E+00	9.055E+01
0.04	0.15	6.00	6.008E+01	4.162E-02	1.472E+00	6.160E+01
0.05	0.19	7.00	4.266E+01	3.479E-02	1.411E+00	4.410E+01
0.06	0.22	9.00	3.142E+01	2.959E-02	1.373E+00	3.283E+01
0.07	0.26	10.00	2.387E+01	2.552E-02	1.334E+00	2.523E+01
0.08	0.30	12.00	1.859E+01	2.227E-02	1.300E+00	1.991E+01
0.09	0.33	13.00	1.477E+01	1.967E-02	1.268E+00	1.606E+01
0.10	0.37	15.00	1.195E+01	1.753E-02	1.236E+00	1.320E+01
0.20	0.74	29.00	2.781E+00	8.622E-03	1.032E+00	3.821E+00
0.30	1.11	44.00	1.191E+00	5.951E-03	9.200E-01	2.117E+00
0.40	1.48	58.00	6.660E-01	4.589E-03	8.468E-01	1.517E+00
0.50	1.85	73.00	4.268E-01	3.742E-03	7.885E-01	1.219E+00
0.60	2.22	87.00	2.915E-01	3.170E-03	7.501E-01	1.045E+00
0.80	2.96	117.00	1.497E-01	2.451E-03	6.962E-01	8.483E-01
1.00	3.70	146.00	7.871E-02	2.012E-03	6.534E-01	7.341E-01
1.25	4.63	182.00	2.860E-02	1.654E-03	6.189E-01	6.492E-01
1.50	5.56	219.00	6.463E-03	1.412E-03	5.844E-01	5.923E-01
1.75	6.48	255.00	1.053E-03	1.238E-03	5.595E-01	5.617E-01
2.00	7.41	292.00	1.032E-04	1.105E-03	5.386E-01	5.398E-01
2.50	9.26	365.00	0.000E+00	9.225E-04	5.008E-01	5.017E-01
3.00	11.11	437.00	0.000E+00	8.022E-04	4.704E-01	4.712E-01
3.50	12.96	510.00	0.000E+00	7.156E-04	4.386E-01	4.393E-01
4.00	14.81	583.00	0.000E+00	6.485E-04	4.140E-01	4.146E-01
4.50	16.67	656.00	0.000E+00	5.942E-04	3.923E-01	3.929E-01
5.00	18.52	729.00	0.000E+00	5.490E-04	3.710E-01	3.715E-01
6.00	22.22	875.00	0.000E+00	4.770E-04	3.345E-01	3.350E-01
8.00	29.63	1167.00	0.000E+00	3.795E-04	2.797E-01	2.801E-01
10.00	37.04	1458.00	0.000E+00	3.118E-04	2.381E-01	2.384E-01

Table 6 Daily Dose, 60 Degrees/500 km, Solar Minimum

S GM/SQCM	T MM	T MILS	ELEC RADS-AL	BREM RADS-AL	PROTON RADS-AL	TOTAL RADS-AL
0.01	0.04	1.00	4.304E+02	1.679E-01	6.493E+01	4.955E+02
0.02	0.07	3.00	2.406E+02	1.187E-01	2.498E+01	2.657E+02
0.03	0.11	4.00	1.539E+02	9.230E-02	1.545E+01	1.694E+02
0.04	0.15	6.00	1.076E+02	7.633E-02	1.071E+01	1.184E+02
0.05	0.19	7.00	7.992E+01	6.540E-02	7.814E+00	8.780E+01
0.06	0.22	9.00	6.208E+01	5.710E-02	6.268E+00	6.841E+01
0.07	0.26	10.00	4.989E+01	5.060E-02	5.159E+00	5.510E+01
0.08	0.30	12.00	4.115E+01	4.537E-02	4.395E+00	4.559E+01
0.09	0.33	13.00	3.468E+01	4.110E-02	3.844E+00	3.857E+01
0.10	0.37	15.00	2.967E+01	3.756E-02	3.389E+00	3.310E+01
0.20	0.74	29.00	1.090E+01	2.170E-02	1.675E+00	1.260E+01
0.30	1.11	44.00	6.208E+00	1.625E-02	1.164E+00	7.389E+00
0.40	1.48	58.00	4.088E+00	1.316E-02	9.099E-01	5.011E+00
0.50	1.85	73.00	2.833E+00	1.104E-02	7.575E-01	3.601E+00
0.60	2.22	87.00	2.008E+00	9.501E-03	6.737E-01	2.691E+00
0.80	2.96	117.00	1.056E+00	7.438E-03	5.723E-01	1.636E+00
1.00	3.70	146.00	5.778E-01	6.156E-03	5.052E-01	1.089E+00
1.25	4.63	182.00	2.756E-01	5.123E-03	4.589E-01	7.396E-01
1.50	5.56	219.00	1.309E-01	4.425E-03	4.216E-01	5.570E-01
1.75	6.48	255.00	6.178E-02	3.921E-03	3.964E-01	4.621E-01
2.00	7.41	292.00	2.811E-02	3.540E-03	3.764E-01	4.081E-01
2.50	9.26	365.00	4.293E-03	3.016E-03	3.411E-01	3.484E-01
3.00	11.11	437.00	4.175E-04	2.677E-03	3.140E-01	3.171E-01
3.50	12.96	510.00	8.088E-06	2.436E-03	2.882E-01	2.907E-01
4.00	14.81	583.00	0.000E+00	2.251E-03	2.689E-01	2.711E-01
4.50	16.67	656.00	0.000E+00	2.099E-03	2.524E-01	2.545E-01
5.00	18.52	729.00	0.000E+00	1.970E-03	2.364E-01	2.384E-01
6.00	22.22	875.00	0.000E+00	1.756E-03	2.098E-01	2.116E-01
8.00	29.63	1167.00	0.000E+00	1.453E-03	1.706E-01	1.721E-01
10.00	37.04	1458.00	0.000E+00	1.233E-03	1.421E-01	1.433E-01

from electrons and protons includes both ionization and nonionization. Effects of electron exposure in virtually all modern microcircuits are dominated by accumulated ionization. Definition of the internal ionizing radiation environment in terms of rads(Si) is generally adequate. Failure levels resulting from accumulated ionization can be as low as approximately 1000 rads(Si) for very sensitive unhardened microcircuits to greater than 10 Megarads(Si) for hardened microcircuits [15].

Effects of proton exposure over the energy range of interest in the space environment include both ionization and atomic displacement damage [16]. Failure levels resulting from proton-induced displacement damage can be as low as 1E10 p/cm^2 for very sensitive bipolar analog microcircuits or power transistors. In general, however, effects of proton exposure on the internal electronics are dominated by the ionizing energy deposition [15]. Definition of the proton environment for the internal electronics should include

Table 7 Daily Dose, 90 Degrees/500 km, Solar Minimum

S GM/SQCM	T MM	T MILS	ELEC RADS-AL	BREM RADS-AL	PROTON RADS-AL	TOTAL RADS-AL
0.01	0.04	1.00	3.693E+02	1.449E-01	4.279E+01	4.123E+02
0.02	0.07	3.00	2.123E+02	1.049E-01	1.725E+01	2.297E+02
0.03	0.11	4.00	1.395E+02	8.307E-02	1.090E+01	1.504E+02
0.04	0.15	6.00	9.986E+01	6.959E-02	7.660E+00	1.076E+02
0.05	0.19	7.00	7.573E+01	6.027E-02	5.652E+00	8.144E+01
0.06	0.22	9.00	5.986E+01	5.315E-02	4.573E+00	6.449E+01
0.07	0.26	10.00	4.885E+01	4.748E-02	3.789E+00	5.269E+01
0.08	0.30	12.00	4.079E+01	4.288E-02	3.247E+00	4.408E+01
0.09	0.33	13.00	3.471E+01	3.907E-02	2.855E+00	3.761E+01
0.10	0.37	15.00	2.997E+01	3.586E-02	2.529E+00	3.254E+01
0.20	0.74	29.00	1.127E+01	2.103E-02	1.287E+00	1.258E+01
0.30	1.11	44.00	6.340E+00	1.573E-02	9.079E-01	7.263E+00
0.40	1.48	58.00	4.096E+00	1.270E-02	7.170E-01	4.826E+00
0.50	1.85	73.00	2.789E+00	1.062E-02	6.008E-01	3.400E+00
0.60	2.22	87.00	1.948E+00	9.110E-03	5.356E-01	2.493E+00
0.80	2.96	117.00	1.001E+00	7.104E-03	4.559E-01	1.464E+00
1.00	3.70	146.00	5.370E-01	5.874E-03	4.019E-01	9.448E-01
1.25	4.63	182.00	2.496E-01	4.890E-03	3.644E-01	6.189E-01
1.50	5.56	219.00	1.148E-01	4.227E-03	3.351E-01	4.541E-01
1.75	6.48	255.00	5.203E-02	3.751E-03	3.153E-01	3.711E-01
2.00	7.41	292.00	2.264E-02	3.392E-03	3.003E-01	3.263E-01
2.50	9.26	365.00	3.159E-03	2.896E-03	2.740E-01	2.800E-01
3.00	11.11	437.00	2.841E-04	2.573E-03	2.538E-01	2.567E-01
3.50	12.96	510.00	4.912E-06	2.344E-03	2.340E-01	2.363E-01
4.00	14.81	583.00	0.000E+00	2.168E-03	2.187E-01	2.209E-01
4.50	16.67	656.00	0.000E+00	2.022E-03	2.056E-01	2.076E-01
5.00	18.52	729.00	0.000E+00	1.899E-03	1.927E-01	1.946E-01
6.00	22.22	875.00	0.000E+00	1.694E-03	1.713E-01	1.730E-01
8.00	29.63	1167.00	0.000E+00	1.402E-03	1.396E-01	1.410E-01
10.00	37.04	1458.00	0.000E+00	1.191E-03	1.165E-01	1.177E-01

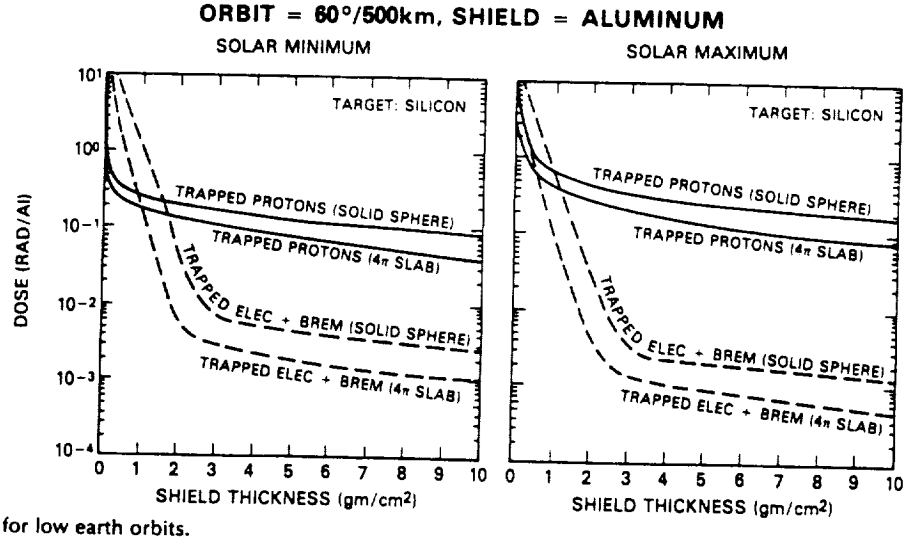

Fig. 14. Daily dose for low earth orbits.

both the proton-induced energy deposition (in rads(Si)), and the internal proton fluence and energy spectra for accurate characterization.

D. Single Event Susceptibility of Electronics

The high energy protons of the trapped space radiation environment can cause single event effects in modern semiconductor electronics. The proton energy threshold for these effects is approximately 10 MeV, with the cross section for nuclear reactions increasing substantially at 30 MeV and above [16]. Typically, a nuclear reaction resulting in a single event occurs on the order of once for every 100 000 protons. In terms of microcircuit susceptibility, for a 60° orbit, the maximum proton-induced upset rate occurs in the heart of the proton trapping domain of the radiation belts at an altitude of approximately 2600 km. It has been estimated that for electronics with "typical" shielding, the single event upset rate could be as high as 0.1 upsets/bit-day for very susceptible microcircuit technologies, decreasing by at least five orders of magnitude for less susceptible microcircuit technologies [17].

At low altitudes, low inclination orbits, the proton-induced single event upset rate is determined by passages through the South Atlantic Anomaly. During the flux-free times, the electronics will be free of single event upsets from trapped protons. The confinement of proton-induced upsets to passages through the SAA may be either an advantage or handicap to overall satellite system hardening.

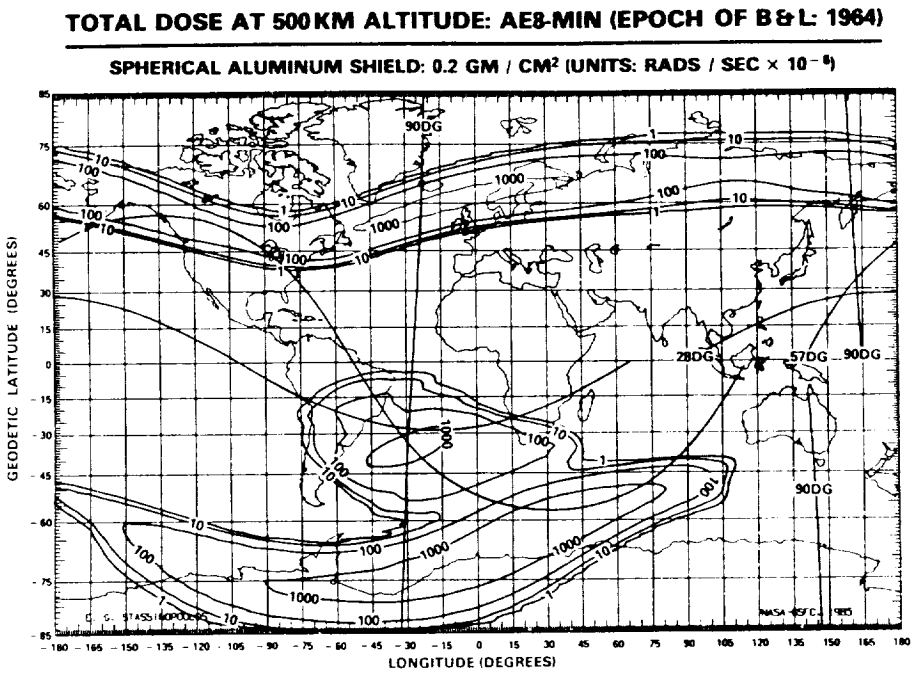

Fig. 15. World map contours of total dose: shield thickness = 0.2 gm/cm^2.

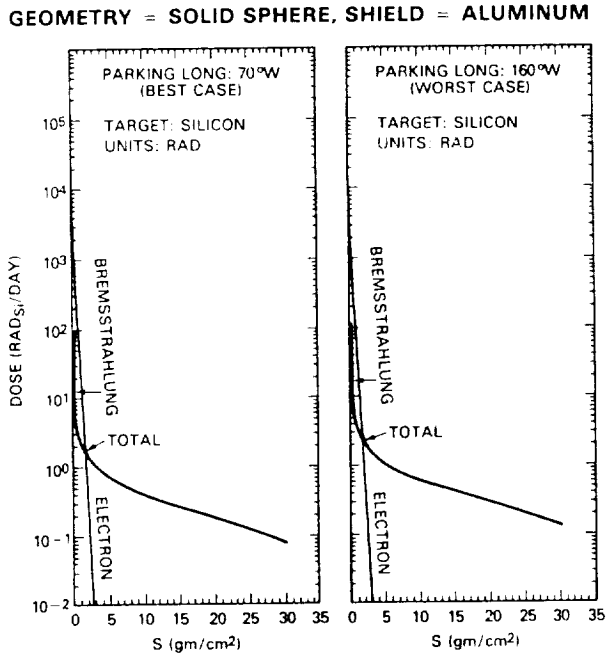

Fig. 16. Daily electron doses for geostationary orbits.

III. Transiting Radiation

The transiting radiation of the space radiation environment is composed of a solar contribution and a galactic contribution. Each is composed of high energy protons and heavy ions. In terms of the spacecraft electronics, the dominant effects are those associated with the ionization tracks of single particles, as well as the effects of total accumulated ionization. As with the trapped radiation environment, we will first present the external environment, then the internal environment, and finally comment on the effects in the spacecraft electronics.

A. Solar Cosmic Rays

1) Solar Flare Protons: Disturbed regions on the sun sporadically emit bursts of energetic charged particles into interplanetary space. These solar energetic particle (SEP) events (usually occurring in association with solar flares) are composed primarily of protons, with a minor constituent of alpha particles (5–10 percent), heavy ions, and electrons. The emission of protons from the SEP event can last as long as several days.

The time history of energetic solar flare particles as they arrive at the earth after the occurrence of the parent flare has several important characteristics. First, the particles arrive in tens of minutes to several hours (depending on their energy and point of origin on the sun); second, they peak within two hours to one day; and third, they decay within a few days to one week. It is important to note that the most energetic protons arrive at the earth in about 10–30 minutes.

SEP event phenomenology distinguishes between ordinary (OR) events and anomalously-large (AL) events. AL events are quite rare. Fig. 17 shows the energetic solar flare proton events since 1956. As shown, three AL events occurred during the 19th solar cycle, one during the 20th cycle, and none in the 21st cycle [18]. They occur mostly near the first and last year of the solar maximum phase. The prediction of AL events was initially based on an empirical model [3], and later on a probabilistic treatment involving modified Poisson statistics [19]. A simple statistical predictive model for solar flares is provided by SOLPRO [20], which is based exclusively on satellite spectral measurements covering nearly the entire 20th solar cycle. This model predicts, for a given mission duration and a specified confidence

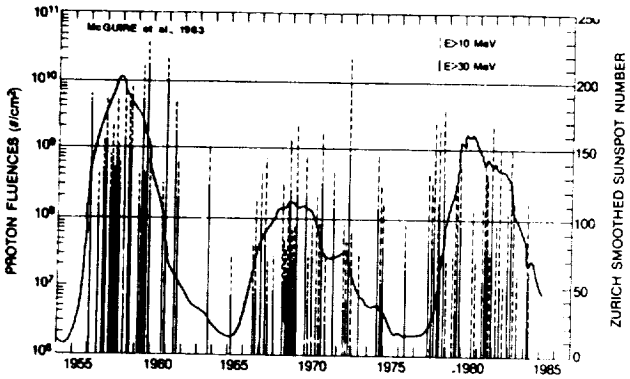

Fig. 17. Solar flare proton events for solar cycles 19, 20, and 21.

level, the mission integrated proton fluence spectrum from OR events, and the number of AL events to be expected with their event-integrated fluence spectra. In terms of proton fluence, since AL events are rare, small-sample statistics are the only appropriate prediction technique. Thus, for spacecraft of mission durations greater than one year, OR event fluences are not significant, because probability theory predicts the occurrence of at least one AL event, even for a confidence level as low as 80 percent.

2) Solar Heavy Ions: For ordinary solar flare events, the relative abundance of the helium ions in the emitted particle fluxes is usually between 5 and 10 percent, while the fluxes of heavier ions are very small, and significantly below the galactic background. However, during major solar events, the abundance of some heavy ions may increase rapidly by three or four orders of magnitude above the galactic background, for periods of several hours to days. The increased flux of the heavy ions can have serious consequences in terms of an increased frequency of single event effects within the spacecraft electronics.

B. Galactic Cosmic Rays

The region outside the solar system in the outer part of the galaxy is believed to be filled uniformly with cosmic rays. These consist of about 85 percent protons, about 14 percent alpha particles, and about 1 percent heavier nuclei. The galactic cosmic rays range in energy to above 10 GeV per nucleon. Fig. 18 shows the spectral distributions for hydrogen, helium, carbon, and oxygen ions. The differential energy spectra of the cosmic rays near the earth tend to peak around 1 GeV/nucleon. Toward lower energies, the spectral shape is depressed by interactions with the solar wind and the interplanetary magnetic field. This reduction in flux becomes more pronounced during the active phase of the solar cycle. The total flux of cosmic ray particles seen outside the magnetosphere at the distance of the earth from the sun (i.e., 1 AU) is approximately 4 per square-centimeter per second (primarily composed of protons). For all practical purposes, the cosmic ray flux can be considered as omnidirectional, except for very low altitude orbits, where the solid angle subtended by the earth defines a region free from these particles. Fig. 19 shows the relative abundances of the galactic cosmic ray ions. A model for these particles is available [21].

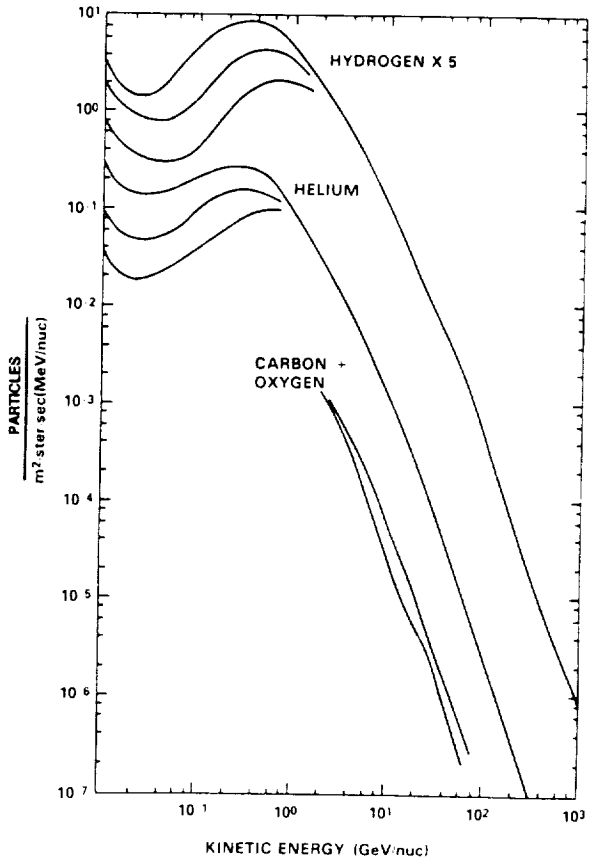

Fig. 18. Cosmic ray spectral distributions.

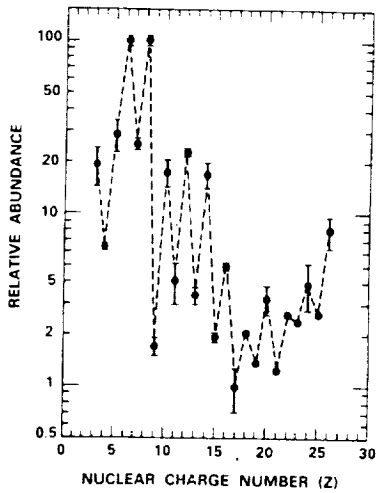

Fig. 19. Relative abundance of nuclei in the galactic cosmic radiation.

C. Geomagnetic Shielding

Low altitude and latitude earth orbits are essentially shielded from solar or galactic cosmic rays by the geomagnetic field up to inclinations of about 45°. The earth's field acts as an energy filter preventing particles with less than given momentum values from penetrating to certain altitude-latitude combinations. Figs. 20 and 21 show the total ion energy required to penetrate the magnetosphere in

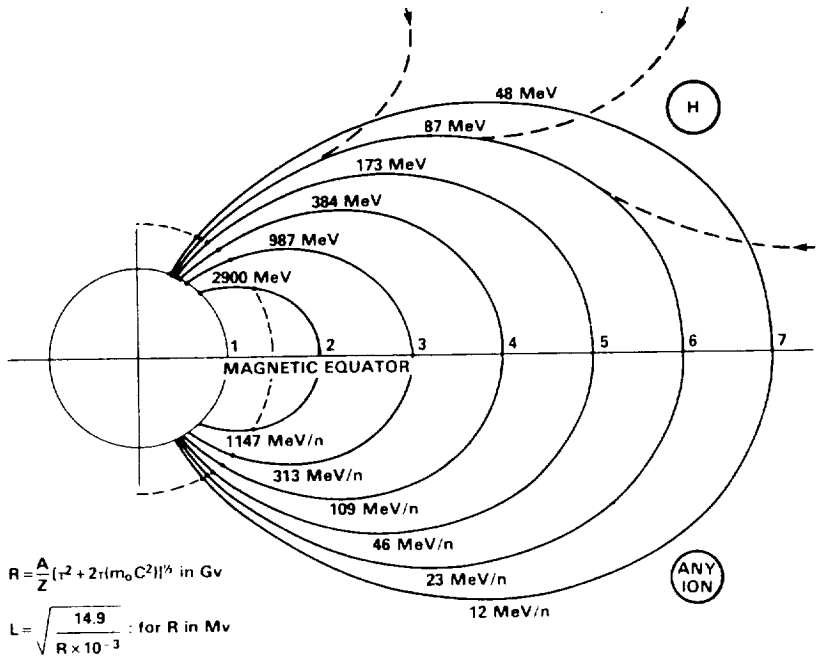

Fig. 20. Total energy required to penetrate the magnetosphere.

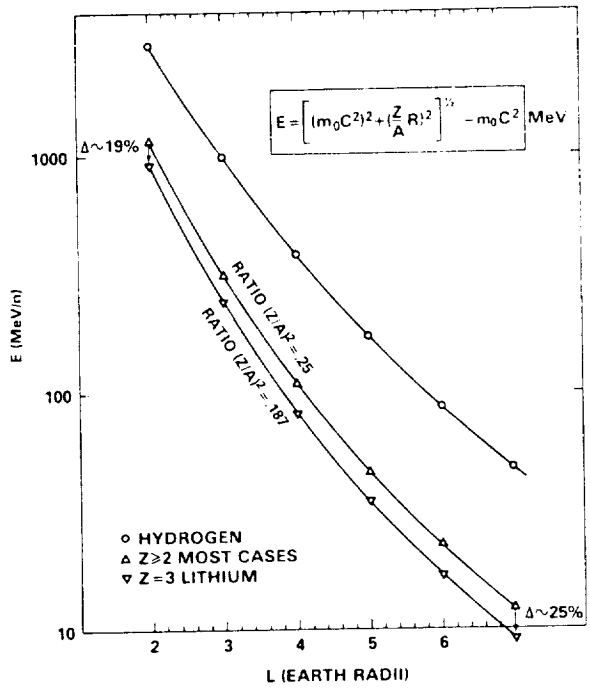

Fig. 21. Total energy required to penetrate the magnetosphere.

terms of the dipole parameter *L*. Table 8 and Fig. 22 show the effects of geomagnetic shielding on solar flare protons for high inclination (greater than 60°) low earth orbits. Fig. 23 shows the effect of shielding on cosmic ray silicon atoms for low earth orbits. Fig. 24 shows the magnetospheric attenuation dependence of the galactic cosmic ray iron spectrum on energy and *L*.

For geostationary orbits, magnetic shielding is relatively ineffective, and such orbits will be exposed to galactic

Table 8 Solar Flare Proton Fluences, 1 AL, Altitude = 500 km

ENERGY (>MEV)	1 AL UNATTEN #/SQCM*EVENT	28.5 DEG #/SQCM*EVENT	60 DEG #/SQCM*EVENT	90 DEG #/SQCM*EVENT
10.0	1.680E+10	0	5.314E+08	3.837E+09
20.0	1.152E+10	-	4.429E+08	2.761E+09
30.0	7.900E+09	-	3.502E+08	1.960E+09
40.0	5.417E+09	-	2.554E+08	1.386E+09
50.0	3.714E+09	-	1.996E+08	9.735E+08
60.0	2.547E+09	-	1.461E+08	6.819E+08
70.0	1.746E+09	-	1.062E+08	4.762E+08
80.0	1.197E+09	-	7.717E+07	3.322E+08
90.0	8.210E+08	-	5.516E+07	2.316E+08
100.0	5.629E+08	-	3.903E+07	1.608E+08
110.0	3.860E+08	-	2.762E+07	1.117E+08
120.0	2.646E+08	-	1.976E+07	7.766E+07
130.0	1.815E+08	-	1.417E+07	5.389E+07
140.0	1.244E+08	-	1.011E+07	3.723E+07
150.0	8.531E+07	-	7.225E+06	2.571E+07
160.0	5.850E+07	-	5.177E+06	1.779E+07
170.0	4.011E+07	-	3.696E+06	1.231E+07
180.0	2.750E+07	-	2.610E+06	8.508E+06
190.0	1.886E+07	-	1.827E+06	5.874E+06
200.0	1.293E+07	0	1.276E+06	4.056E+06

cosmic ray hydrogen of energies above approximately 60 MeV, and heavier ions above 15 MeV per nucleon. This is illustrated in Table 9 for energetic solar flare protons, and is independent of parking longitude.

Geomagnetic shielding effects on geocentric missions are usually evaluated with simple rigidity considerations, for economy reasons, and because of substantial diurnal variations in the cutoff latitudes associated with geomagnetic tail effects (2–4 degrees), and storm-induced changes (>4 degrees).

IV. Transiting Radiation Transport, Shielding, and Energy Deposition

A. Emerging Radiation Spectra

1) Solar Flare Protons: Considerations in the transport of solar flare protons are similar to those previously discussed

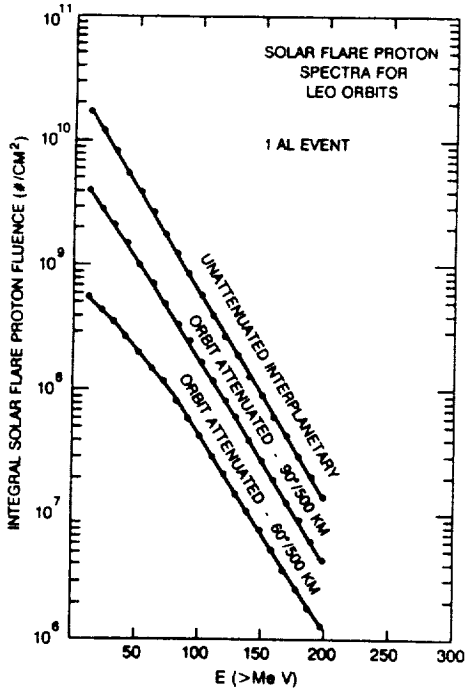

Fig. 22. Magnetospheric attenuation of solar flare protons for LEO.

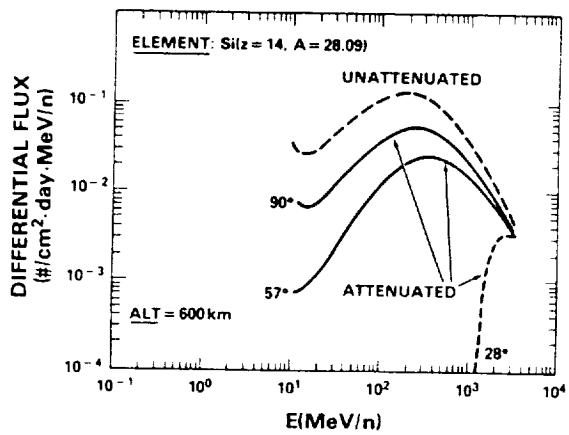

Fig. 23. Magnetospheric attenuation of cosmic rays for LEO.

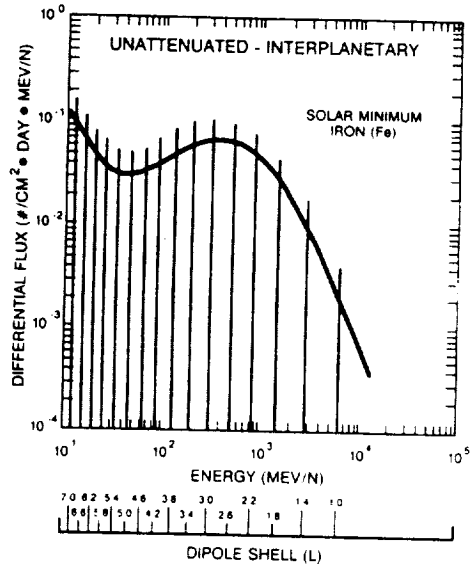

Fig. 24. Dependence of the attenuation of galactic cosmic rays on energy and L.

Table 9 Solar Flare Proton Fluences, 1 AL, GEO

ENERGY (>MEV)	1 AL UNATTEN #/SQCM*EVENT	ENERGY (>MEV)	1 AL 160 W #/SQCM*EVENT	ENERGY (>MEV)	1 AL 70 W #/SQCM*EVENT
10.0	1.680E+10	NOT ACCESSIBLE		NOT ACCESSIBLE	
20.0	1.152E+10		0		0
30.0	7.900E+09		0		0
40.0	5.417E+09	48.1	3.990E+09		0
50.0	3.714E+09	50.0	3.714E+09		0
60.0	2.547E+09	60.0	2.547E+09	60.4	2.509E+09
70.0	1.746E+09	70.0	1.746E+09	70.0	1.746E+09
80.0	1.197E+09	80.0	1.197E+09	80.0	1.197E+09
90.0	8.210E+08	90.0	8.210E+08	90.0	8.210E+08
100.0	5.629E+08	100.0	5.629E+08	100.0	5.629E+08
110.0	3.860E+08	110.0	3.860E+08	110.0	3.860E+08
120.0	2.646E+08	120.0	2.646E+08	120.0	2.646E+08
130.0	1.815E+08	130.0	1.815E+08	130.0	1.815E+08
140.0	1.244E+08	140.0	1.244E+08	140.0	1.244E+08
150.0	8.531E+07	150.0	8.531E+07	150.0	8.531E+07
160.0	5.850E+07	160.0	5.850E+07	160.0	5.850E+07
170.0	4.011E+07	170.0	4.011E+07	170.0	4.011E+07
180.0	2.750E+07	180.0	2.750E+07	180.0	2.750E+07
190.0	1.886E+07	190.0	1.886E+07	190.0	1.886E+07
200.0	1.293E+07	200.0	1.293E+07	200.0	1.293E+07

for the trapped protons. The materially attenuated emerging spectra reflect the shielding effect on the distribution of the solar flare protons, as shown in Fig. 25. The proton fluxes in the 0.1 to 10 MeV range emerging behind spherical aluminum shields of thickness ranges from 0.3 to 5 grams/cm^2 are substantial. Particularly relevant to single particle event effects in the electronics is the Linear Energy Transfer (LET) in silicon, defined as the energy deposition per unit length in the active region of the semiconductor device. The LET spectrum for one AL event is shown in Fig. 26 for the interplanetary solar flare proton spectrum not attenuated by the magnetosphere, emerging from spherical aluminum shields of two thicknesses. Stopping powers (dE/dx) were calculated from the classical equation [22]. The Bethe formula is accurate to about 20 percent at a few MeV per nucleon [23]. The error decreases at higher energies, where the assumptions of the Bethe formulation are increasingly valid. At energies below a few MeV per nucleon, the error increases due to unmodeled details of the energy loss mechanisms.

In general, the ionization loss of a single proton is insufficient to cause a single event effect in a semiconductor device. Observed single event effects from proton exposures are the result of the energy deposition of particles produced by nuclear interactions by the incident proton with the target nucleus. The proton threshold energy for these nuclear interactions is approximately 30 MeV [17].

2) Galactic Cosmic Rays: Fig. 27 shows the unattenuated interplanetary spectra for silicon cosmic ray ions, the magnetospherically attenuated orbit-integrated spectra incident on the surface of the spacecraft, and the shielded spectra of emerging particles behind selected thicknesses of spherical aluminum geometries for an orbit of 57° inclination and 600 km altitude. Differential particle fluxes are shown referenced to the left ordinate. Also shown in Fig. 27 is the Linear Energy Transfer (LET) spectrum of the silicon

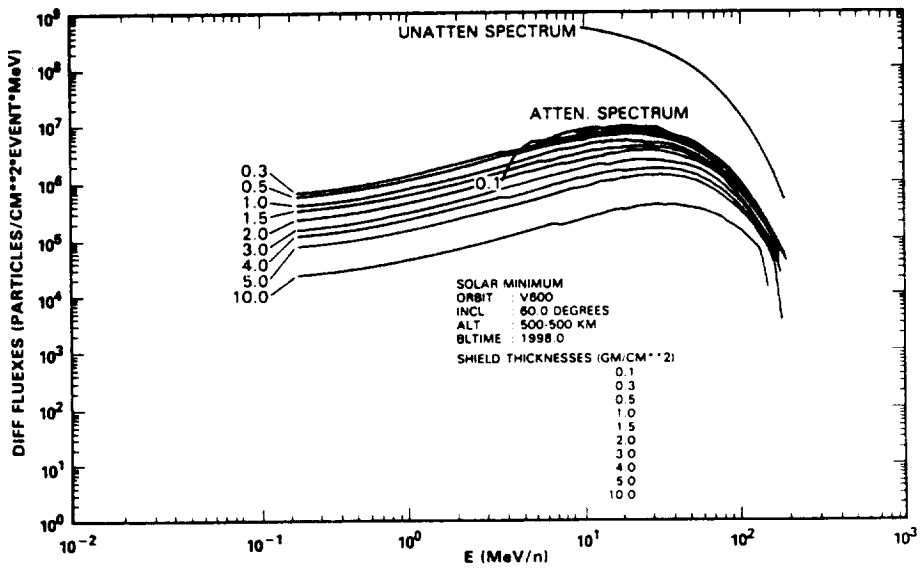

Fig. 25. Emerging solar flare proton spectra, given for 1 AL event, behind spherical aluminum shields.

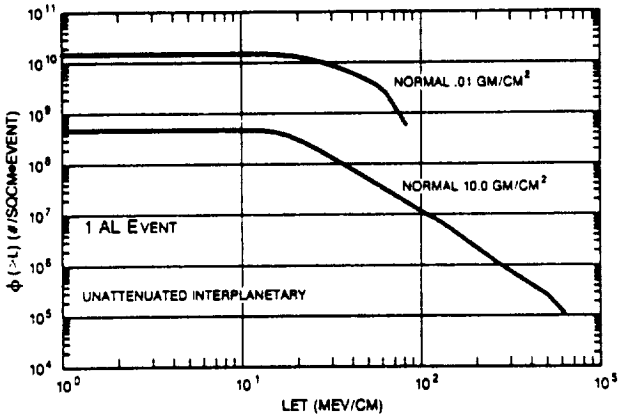

Fig. 26. Integral LET spectra for solar flare protons behind spherical aluminum shields.

ion as a function of energy, referenced to the right ordinate. The LET spectrum is important in defining the energy deposited by a single particle, and subsequent single event effects in the spacecraft electronics.

In passing through shielding material, nuclear reactions are induced by heavy ions with energies above an effective threshold of a few MeV/nucleon. These nuclear reactions provide a source of secondary radiation, both prompt and delayed. Above several hundred MeV/nucleon, nuclear reactions surpass atomic ionization as the main attenuation mechanism in material. At higher energies, the interaction of the incident particle tends to occur primarily with individual nucleons in the target nucleus, and can lead to the ejection of several energetic protons and neutrons. This "spallation" process leaves the product nucleus highly excited, with de-excitation occurring through the "evaporation" of additional nucleons and the emission of gamma

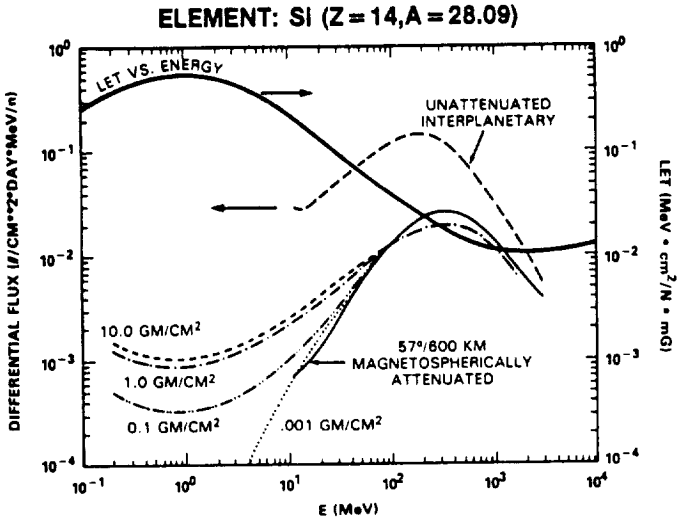

Fig. 27. Galactic cosmic ray spectra (solar min.) emerging behind spherical aluminum shields.

rays. For 400 MeV protons incident on aluminum, the average total nuclear emission is 4.8, including 2.8 spallation nucleons with an average energy of 120 MeV [24]. The process can generate a rich variety of residual nuclei, especially in heavier elements, as a result of the multiplicity of statistically possible reaction paths (i.e., the specific number of protons and neutrons emitted). These product nuclei frequently are radioisotopes decaying by beta-ray emission with a variety of lifetimes.

Several important features are illustrated by the curve of Fig. 28. First, there is substantial attenuation by the earth's magnetic field of all particles in the energy range of 10–10 000 MeV per nucleon. Second, there is an insignificant effect of material shielding in the energy range from about 90 to 10 000 MeV. Note that there is no substantial decrease in flux even for aluminum shielding of 10 grams/cm^2 (approximately 1.5 inches). Third, there is an unavoidable shield side effect of a significant increase in the low energy (0.8–50 MeV/nucleon) high-LET fluxes for shield thickness greater than 0.1 gram/cm^2 of aluminum. With increasing shield thicknesses, the population of high energy ions decreases slightly, but with a resultant increase in the low energy (0.8–50 MeV/nuclear) ions. Since the LET increases with decreasing energy in this range (heavy solid curve) the presence of the shield actually increases the severity of the environment to the internal electronics.

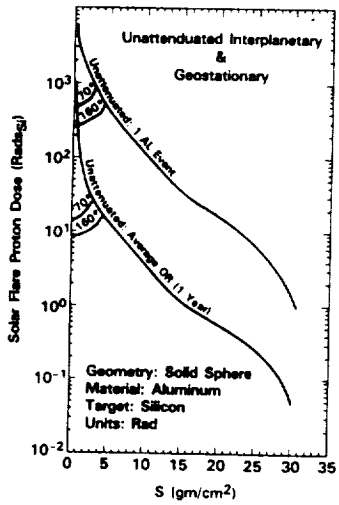

Fig. 28. Solar flare proton dose.

B. *Ionizing Radiation Dose*

In general, the ionizing radiation dose from the transiting radiation environment is not significant compared to that of the trapped radiation environment. Particle fluxes from energetic solar flares are heavily attenuated by the geomagnetic field, which prevents their penetration to low orbital altitudes and inclinations. For a 500 km, 30° inclination orbit, the attenuation is nearly total. In a 500 km, 57° inclination orbit, some penetration occurs. In contrast, a polar orbit experiences a substantial degree of exposure at any altitude.

In GEO, the geomagnetic shielding is relatively ineffective. Even so, the average yearly dose from ordinary (OR) events behind a 2 gram/cm^2 spherical aluminum shield is quite small, approximately 18 rads(Si)/year. In comparison,

Table 10 Solar Flare Shielded Dose, 1 AL, GEO

	MAGNETOSPHERICALLY UNATTENUATED		MAGNETOSPHERICALLY ATTENUATED TO 70DEG W		MAGNETOSPHERICALLY ATTENUATED TO 160DEG W	
S (GM/SQCM)	SLAB(4PI) (RADS-SI)	SOLID SPHERE (RADS-SI)	SLAB(4PI) (RADS-SI)	SOLID SPHERE (RADS-SI)	SLAB(4PI) (RADS-SI)	SOLID SPHERE (RADS-SI)
0.01	4.690E+03	4.597E+03	4.796E+02	4.782E+02	2.680E+02	2.675E+02
0.02	4.762E+03	4.645E+03	4.810E+02	4.781E+02	2.686E+02	2.674E+02
0.03	4.812E+03	4.688E+03	4.824E+02	4.782E+02	2.692E+02	2.675E+02
0.04	4.846E+03	4.737E+03	4.838E+02	4.784E+02	2.696E+02	2.675E+02
0.05	4.868E+03	4.788E+03	4.850E+02	4.786E+02	2.702E+02	2.676E+02
0.06	4.878E+03	4.850E+03	4.862E+02	4.788E+02	2.708E+02	2.676E+02
0.08	4.872E+03	4.950E+03	4.886E+02	4.794E+02	2.718E+02	2.678E+02
0.10	4.828E+03	5.221E+03	4.910E+02	4.802E+02	2.728E+02	2.680E+02
0.20	4.004E+03	5.875E+03	5.000E+02	4.849E+02	2.768E+02	2.696E+02
0.30	3.202E+03	5.117E+03	5.062E+02	4.902E+02	2.802E+02	2.716E+02
0.40	2.680E+03	4.429E+03	5.110E+02	4.950E+02	2.826E+02	2.737E+02
0.50	2.298E+03	3.957E+03	5.144E+02	4.998E+02	2.846E+02	2.758E+02
0.60	2.004E+03	3.553E+03	5.168E+02	5.051E+02	2.862E+02	2.776E+02
0.70	1.774E+03	3.216E+03	5.182E+02	5.108E+02	2.874E+02	2.794E+02
0.80	1.587E+03	2.966E+03	5.190E+02	5.168E+02	2.884E+02	2.814E+02
0.90	1.428E+03	2.727E+03	5.188E+02	5.232E+02	2.892E+02	2.836E+02
1.00	1.296E+03	2.512E+03	5.180E+02	5.297E+02	2.898E+02	2.860E+02
1.25	1.038E+03	2.134E+03	5.130E+02	5.488E+02	2.900E+02	2.921E+02
1.50	8.504E+02	1.795E+03	5.038E+02	5.690E+02	2.890E+02	2.988E+02
1.75	7.120E+02	1.592E+03	4.908E+02	6.002E+02	2.868E+02	3.061E+02
2.00	5.978E+02	1.402E+03	4.736E+02	6.153E+02	2.834E+02	3.144E+02
2.50	4.430E+02	1.037E+03	4.244E+02	7.829E+02	2.736E+02	3.334E+02
3.00	3.424E+02	8.769E+02	3.406E+02	8.544E+02	2.592E+02	3.626E+02
3.50	2.654E+02	7.021E+02	2.654E+02	6.989E+02	2.394E+02	3.929E+02
4.00	2.136E+02	5.719E+02	2.136E+02	5.725E+02	2.118E+02	4.972E+02
4.50	1.733E+02	4.956E+02	1.733E+02	4.954E+02	1.733E+02	5.004E+02
5.00	1.418E+02	4.160E+02	1.418E+02	4.161E+02	1.418E+02	4.147E+02
6.00	9.860E+01	3.047E+02	9.860E+01	3.047E+02	9.860E+01	3.050E+02
8.00	5.120E+01	1.759E+02	5.120E+01	1.759E+02	5.120E+01	1.759E+02
10.00	2.870E+01	1.094E+02	2.870E+01	1.094E+02	2.870E+01	1.094E+02
15.00	7.984E+00	3.464E+01	7.984E+00	3.464E+01	7.984E+00	3.464E+01
20.00	2.558E+00	1.580E+01	2.558E+00	1.580E+01	2.558E+00	1.580E+01
30.00	1.104E-01	1.250E+00	1.104E-01	1.250E+00	1.104E-01	1.250E+00

the event-integrated dose from an anomalously large (AL) flare at parking longitude of 70° W would be approximately 600 rads(Si)/event for the same shield and target as shown in Fig. 28 and Table 10. Tripling the shield thickness to 6 grams/cm^2 would result in 300 rads/event.

C. *Single Event Susceptibility of Electronics*

Single event upset effects in electronics from the transiting space radiation environment may be the result of either the energetic solar flare protons or cosmic rays. The nature of trapped proton-induced single event effects has been discussed previously. In general, the single event upset rate due to transiting protons is small compared to that due to cosmic rays, except for the occurrence of an AL. To cover the occurrence of an AL during the spacecraft mission, both the expected duration and fluence of the AL must be considered in the electronics design.

For the cosmic ray component of the transiting space radiation environment, the definition of the LET spectrum of the internal radiation environment is a fundamental basis for characterization of component susceptibility. Observed effects from single heavy high energy ions include memory bit upset, microprocessor errors, CMOS latchup and burnout in power MOSFETs, and electrically-erasable PROMs [25], [26]. The probability of latchup or burnout is much less than that of memory bit upset or logic errors, but the consequences to system operation may be much more severe.

Generally, cosmic-ray-induced single event effects dominate proton-induced single event effects both at altitudes below 1000 km and above 4000 km for 60° circular orbits. For orbits of lower inclinations, the cosmic rays are shielded by the earth's magnetic field, causing the cosmic ray upset level to decrease compared to the proton upset rate. On the other hand, for orbits of higher inclinations, the relative upset rate of the cosmic rays increases. The variations in the spacecraft orbit, space radiation environment, and device susceptibility should be considered in estimating specific cosmic ray/proton upset levels in support of spacecraft electronics design. The specification of the internal electronics environment should include the time-dependent proton flux and energy spectrum, the cosmic ray LET spectrum, and the cosmic ray spectrum by particle species and energy spectrum. The actual cosmic ray spectrum can be a valuable supplement to the LET spectrum in those cases where more detail is necessary to support experimental characterization in ground-based laboratory facilities.

Conclusion

The richly diverse earth space radiation environment has been described in terms of its nature and variations with respect to the susceptibility of spacecraft electronics. The constraints of space radiation effects on spacecraft electronics design can be significant, but with careful component selection, shielding, and design, systems can be realized that are both of high performance and long endurance.

This paper has specifically addressed the earth radiation environment, but our planet is not alone in its magnetic field and trapped radiation belts. Jupiter, to be explored by the Galileo spacecraft, has a trapped radiation environment much more severe than that of the earth. Even in transit to the outer planets and beyond, the galactic cosmic rays must be considered in their effects on the electronics. As our knowledge of the space radiation environments and radiation effects of electronics grows, the electronics technology itself evolves. The combination will be both exciting and challenging for many years to come.

References

[1] D. R. Barraclough, R. M. Harwood, B. R. Leaton, and S. R. C. Malin, "A model of the geomagnetic field at epoch 1975," *Geophys. J. R. Astron. Soc.*, vol. 43, p. 645, 1975.

[2] IAGA Division I, Working Group 1, "International geomagnetic reference field, revision 1985," EOS, vol. 67, pp. 523–524, June 1986.

[3] E. G. Stassinopoulos and J. H. King, "Empirical solar proton model for orbiting spacecraft applications," *IEEE Trans. Aerosp. Electron. Syst.*, vol. AES-10, no. 4, July 1974.

[4] W. N. Spjeldvik and P. L. Rothwell, "The earth's radiation belts," Rep. AFGL-TR-83-0240, Air Force Geophysics Laboratory, Hanscom AFB, MA, Sept. 29, 1983.

[5] C. E. McIlwain, "Coordinates for mapping the distribution of magnetically trapped particles," *J. Geophys. Res.*, vol. 66, no. 11, pp. 3681–3691, 1961.

[6] D. M. Sawyer and J. I. Vette, "AP8 trapped proton environment for solar maximum and solar minimum," Rep. NSSDC 76-06, National Space Science Data Center, Greenbelt, MD, Dec., 1976.

[7] "AE8 trapped electron model," to be published by the National Space Science Data Center, NASA-Goddard Space Flight Center.

[8] L. J. Lanzerotti, C. S. Roberts, and W. L. Brown, "Temporal variations in the electron flux at synchronous altitude," *J. Geophys. Res.*, vol. 72, no. 23, pp. 5893–5902, Dec. 1967.

[9] R. P. Lin and K. A. Anderson, "Periodic modulation of the energetic electron fluxes in the distant radiation zone," *J. Geophys. Res.*, vol. 71, no. 7, pp. 1827–1835; Apr. 1966.

[10] B. J. O'Brein, "A large diurnal variation of the geomagnetically trapped radiation," *J. Geophys. Res.*, vol. 68, no. 4, pp. 989–995; Feb. 1963.

[11] M. J. Teague and E. G. Stassinopoulos, "A model of the Starfish flux in the inner radiation zone," NASA/GSFC Rep. X-601-72-487, Dec. 1972.

[12] E. G. Stassinopoulos and P. Verzariu, "General formula of decay lifetimes of Starfish electrons," *J. Geophys. Res.*, vol. 76, no. 7, pp. 1841–1844, Mar. 1971.

[13] T. M. Jordan, "Adjoint Monte Carlo electron shielding calculations," *ANS Trans.*, vol. 41, June 1982.

[14] S. Seltzer, "SHIELDOSE: A computer code for space shielding radiation dose calculations," U.S. Dep. Commerce, National Bureau of Standards, NBS Technical Note 1116, May 1980.

[15] J. P. Raymond and E. L. Petersen, "Comparison of neutron, proton, and gamma ray effects in semiconductor devices," *IEEE Trans. Nuclear Sci.*, vol. NS-34, no. 6, pp. 1622–1628, Dec. 1987.

[16] E. L. Petersen, "Soft errors due to protons in the radiation belt," *IEEE Trans. Nuclear Sci.*, vol. NS-28, no. 6, pp. 3981–3986; Dec. 1981.

[17] W. L. Bendel and E. L. Petersen, "Proton upsets in orbit," *IEEE Trans. Nuclear Sci.*, vol. NS-30, no. 6, pp. 4481–4485, Dec. 1983.

[18] J. N. Goswami, R. E. McGuire, R. C. Reddy, D. Lai, and R. Jha, "Solar flare protons and alpha particles during the last three solar cycles," submitted to *J. Geophys. R.* (Los Alamos Preprint LA-UR-87-1176).

[19] J. H. King, "Solar proton fluences for 1977–1983 space missions," *J. Spacecraft and Rockets*, vol. 11, pp. 401–408, 1974.

[20] E. G. Stassinopoulos, "SOLPRO: A computer code to calculate probabilistic energetic solar proton fluences," NSSDC Rep. no. 75-11, National Space Science Data Center, Greenbelt, MD, Apr. 1975.

[21] J. H. Adams, R. Silberg, and C. H. Tszo, "Cosmic ray effects on microelectronics, Part I: The near-earth particle environment," Naval Research Laboratory, NRL Mem. Rep. 4506, Aug. 1981.

[22] H. Bethe, "Theory of the passage of fast corpuscular rays through matter," *Ann. Physik*, Ser. 5, pp. 5–325; 1920.

[23] U. Littmark and J. F. Ziegler, *Handbook of Range Distributions for Energetic Ions in all Elements*. New York, NY: Pergamon Press, 1980.
[24] J. W. Haffner, *Radiation and Shielding in Space*. New York, NY: Academic Press, 1967.
[25] D. K. Nichols, L. S. Smith, W. E. Price, R. Koga, and W. A. Kolasinski, "Recent trends in parts SEU susceptibility from heavy ions," *IEEE Trans. Nuclear Sci.*, vol. NS-34, no. 6, pp. 1332-1337, Dec. 1987.
[26] A. E. Waskiewicz, J. W. Groniger, V. H. Strahan, and D. M. Long, "Burnout of power MOS transistors with heavy ions of Californium-252," *IEEE Trans. Nuclear Sci.*, vol. NS-33, no. 6, pp. 1710-1713, Dec. 1986.

of radiation effects in electronic devices; modeling of physical processes in the earth's magnetosphere and in interplanetary space; large-scale data analysis and correlation; space-borne and laboratory scientific and engineering experiments; dosimetry research and applications; etc. He has published over 100 papers and articles in scientific, technical, and engineering journals, books, and official NASA publications.